HHS Public Access

Author manuscript

Cell Stem Cell. Author manuscript; available in PMC 2024 March 02.

Published in final edited form as:

Cell Stem Cell. 2023 March 02; 30(3): 264–282.e9. doi:10.1016/j.stem.2023.02.003.

hPSC-derived Sacral Neural Crest Enables Rescue in a Severe Model of Hirschsprung's Disease

Yujie Fan[1,2,3], **James Hackland**[1,2], **Arianna Baggiolini**[1,2], **Lin Y Hung**[11], **Huiyong Zhao**[4,5], **Paul Zumbo**[6,7], **Polina Oberst**[1,2], **Andrew P. Minotti**[1,2,3], **Emiliano Hergenreder**[1,2,3], **Sarah Najjar**[11], **Zixing Huang**[11], **Nelly M. Cruz**[9], **Aaron Zhong**[1,2,10], **Mega Sidharta**[1,2,10], **Ting Zhou**[1,2,10], **Elisa de Stanchina**[4,5], **Doron Betel**[7,8], **Richard M White**[9], **Michael Gershon**[13], **Kara Gross Margolis**[11,12], **Lorenz Studer**[1,2,14,*]

[1]The Center for Stem Cell Biology, Memorial Sloan Kettering Cancer Center, New York, NY 10065, USA

[2]Developmental Biology Program; Memorial Sloan Kettering Cancer Center, New York, NY 10065, USA

[3]Weill Graduate School of Medical Sciences of Cornell University, New York, NY, 10065, USA

[4]Antitumor Assessment Core Facility, Memorial Sloan Kettering Cancer Center, New York, NY 10065, USA

[5]Molecular Pharmacology Program; Memorial Sloan Kettering Cancer Center, New York, NY 10065, USA

[6]Department of Physiology and Biophysics, Weill Cornell Medicine, New York, NY10065, USA

[7]Applied Bioinformatics Core, Weill Cornell Medicine, New York, NY10065, USA

[8]Division of Hematology and Medical Oncology, Department of Medicine; Weill Cornell Medicine, New York, NY10065, USA

[9]Cancer Biology and Genetics and Department of Medicine, Memorial Sloan Kettering Cancer Center, New York, NY 10065, USA

[10]The SKI Stem Cell Research Facility, Memorial Sloan Kettering Cancer Center, New York, NY 10065, USA

[*]Correspondence to: Lorenz Studer, studerl@mskcc.org.

AUTHOR CONTRIBUTIONS

Y.F. and L.S. developed the experiments and interpreted results. Y.F. performed most experiments and collected and analyzed data. J.H. performed GDF11-related experiments, analysis of RNA seq data and assisted in manuscript preparation. A.B. contributed to sequencing experiments and melanocyte-related experiments and assisted in manuscript preparation. L.Y.H performed the gut motility experiments, whole mount dissections and immunostaining experiments with assistance of S.N and Z.H. K.G.M and M.G helped with experimental design, results and discussion. A.P.M and P.O. performed synapse quantification analysis. H.Z. performed the mouse transplantation studies. P.Z and D.B. performed computational analyses. E.H. performed and analyzed the MEA experiment. N.C performed melanocyte-related experiments. A.Z. M.S and T.Z. generated the reporter lines used in this study. Y.F. and L.S. wrote the manuscript. L.S. acquired funding for the project. All authors read and edited the manuscript.

INCLUSION AND DIVERSITY

We support inclusive, diverse, and equitable conduct of research.

[11]Department of Molecular Pathobiology, New York University College of Dentistry, New York, NY 10010, USA

[12]Department of Pediatrics, NYU Grossman School of Medicine; New York, NY 10010, USA

[13]Department of Pathology and Cell Biology, Columbia University, New York, New York, 10032

[14]Lead contact

Summary:

The enteric nervous system (ENS) is derived from both the vagal and sacral component of the neural crest (NC). Here, we present the derivation of sacral ENS precursors from human PSCs via timed exposure to FGF, WNT and to GDF11, which enables posterior patterning and transition from posterior trunk to sacral NC identity, respectively. Using a *SOX2*::H2B-tdTomato/*T*::H2B-GFP dual reporter hPSC line, we demonstrate that both trunk and sacral NC emerge from a double-positive neuro-mesodermal progenitor (NMP). Vagal and sacral NC precursors yield distinct neuronal subtypes and migratory behaviors *in vitro* and *in vivo*. Remarkably, xenografting of both vagal and sacral NC lineages is required to rescue a mouse model of total aganglionosis, suggesting opportunities in the treatment of severe forms of Hirschsprung's disease.

Graphical Abstract

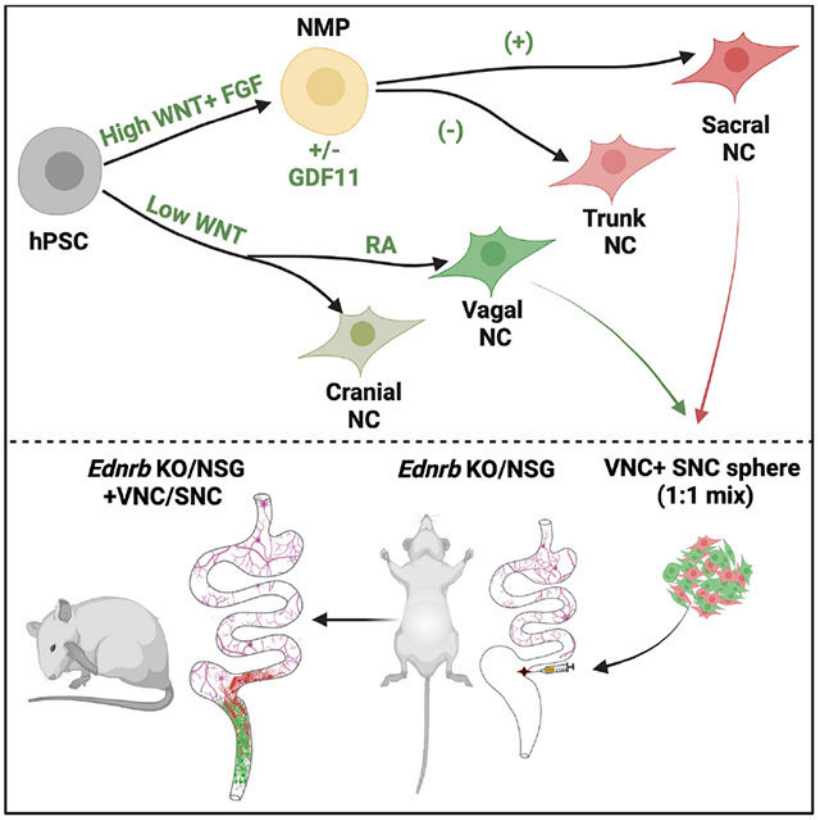

eTOC blurb

Fan and colleagues present a protocol for generating sacral neural crest from human PSCs and compare enteric neuron lineages derived from either sacral or vagal neural crest. Remarkably, rescue of a severe model of Hirschsprung's disease requires the combined injection of sacral and vagal-derived neural crest lineages.

INTRODUCTION:

The enteric nervous system (ENS) is the intrinsic nervous system of the gastrointestinal (GI) tract, which represents a complex network of neurons and glia essential for GI function including motility, food digestion, nutrient absorption, and barrier function[1]. The ENS is derived from the neural crest (NC) during development and represents the largest component of the autonomic nervous system, with > 500 million neurons in humans comprising ~40 distinct neurotransmitter subtypes. Defects in ENS development are responsible for various disorders including Hirschsprung disease (HSCR), a fatal congenital disorder affecting 1:5,000 live births[2]. HSCR is caused by the lack of ENS ganglia in the distal colon[3–5] and in severe cases, loss of ENS ganglia extending into the small intestine[6] (total aganglionosis). Genetic studies have identified many mutations associated with HSCR including mutations of the *EDNRB* or *RET* receptor[7,8]. The ENS may also contribute to CNS disorders including Parkinson disease (PD) and other forms of dementia[9,10]. For example, GI problems commonly precede the onset of PD motor symptoms , and it has been proposed that PD pathology can initiate in the gut with ⟨-synuclein accumulation that spreading from the gut to the brain via the vagal nerve[11,12]. Despite the important roles of the ENS in PNS- and CNS-related diseases, its developmental origin and function remain poorly understood due to the lack of an easily accessible human model system.

During development the ENS is derived from two major NC sources , the vagal NC located anteriorly (somite 1-7), and the sacral NC located posteriorly (caudal to somite 28). The vagal NC is thought to colonize the gut along an anterior to posterior axis. In contrast, the sacral NC is thought to invade the gut caudally, and migrate along a posterior to anterior axis to meet and intermingle with vagal-derived ENS lineages [13]. However, the extent of sacral NC contribution during human ENS development remains unclear. For example, most studies argue that HSCR is caused by defects in the migration of vagal-derived ENS lineages[14]. However, the disease is typically characterized by distal colon aganglionosis, the site where sacral NC invades and likely contributes to distal gut function [15]. Accordingly, it will be important to explore whether sacral-derived ENS lineages may also contribute to HSCR pathogenesis.

Human pluripotent stem cells (hPSCs) present a powerful system to study human ENS development and to access diverse ENS lineages. A first step in generating hPSC-derived ENS precursors is the derivation of NC, which typically involves inhibition of TGFβ signaling, low level BMP activation and activation of WNT signaling. Under these conditions, hPSCs differentiate into cranial NC lacking *HOX* gene expression[16-19]. Combining NC induction with timed exposure to retinoic acid (RA) induces vagal NC specification and differentiation into vagal NC-derived ENS precursors[20]. In contrast, there is limited information on the signals that induce posterior NC with some studies

suggesting a role for WNT and FGF signaling[21,22]. Recent work proposed that posterior NC lineages may emerge from a distinct neuromesodermal progenitor (NMP)[23,24]. NMPs are characterized by co-expression of *Brachyury* and *SOX2* and give rise to both neural and paraxial mesoderm lineages [25,26]. While several studies have reported the derivation of NMP-like cells from mouse or human PSCs[23,26–31], whether NMPs give rise to NC[23,24] remains an unresolved question.

The derivation of both vagal and sacral NC from hPSCs could offer new insights into human development and disease and present therapeutic opportunities in regenerative medicine. Currently, the only effective treatment for HSCR is the surgical removal of the affected aganglionic gut segment. Although lifesaving, the treatment can result in chronic GI dysfunction in some children, and the surgical approach is particularly problematic cases of total aganglionosis[32,33]. The development of cell therapies based on grafting hPSC-derived ENS precursors presents a promising alternative for the treatment of HSCR to mitigate GI dysfunction and to potentially obviate the need for removal surgery completely. We have previously reported a preclinical proof-of-concept by xenografting hESC-derived vagal ENS precursors into the *Ednrb*$^{sl/sl}$ mouse model of HSCR and shown that this approach can prevent HSCR-related death in the transplanted animals[20]. However, the work also raised the question whether complete restoration of ENS function will require the injection of both vagal and sacral derived ENS lineages, and whether a combined transplantation approach could rescue even more severe, total aganglionosis models of HSCR affecting both the large and small intestine.

RESULTS:

Derivation of sacral NC from hPSCs

During development, the NC is generated along the anterior to posterior (AP) axis, giving rise to cranial, vagal, trunk and sacral NC, respectively. Each NC domain shows distinct lineage potential and is characterized by the expression of distinct *HOX* genes[34]. To direct differentiation into sacral NC lineages, we screened candidate patterning factors known to drive posterior fates during embryonic development, including modulators of FGF, WNT and RA signaling. (Figure 1A, S1B). By monitoring expression of both *HOX* genes and key NC markers *SOX10* and *SNAI2*, we found that early exposure to activators of WNT and FGF signaling triggers robust expression of trunk level *HOX* genes without interfering with the expression of NC markers at D20 (Figure 1B, C). Treatment with CHIR99021 (CHIR) and FGF2 further induced expression of *HOX* regulatory genes such as the CDX transcription factors (*CDX1*, *CDX2, CDX4*; Figure S1A). However, despite robust induction of trunk level *HOX* genes, sacral *HOX* genes were not expressed under any of the conditions tested (Figure 1C, right panel). Exposure to RA, in addition to FGF2 and CHIR, did not increase expression of either trunk or sacral *HOX* genes (Figure S1B). These data suggest that additional patterning factors are required to induce sacral NC.

We focused on GDF11 as such a candidate factor. GDF11, also known as BMP11, is a TGFβ family member expressed in the posterior neural tube and tailbud mesoderm[35,36]. GDF11 has been implicated in the trunk to tail transition with *Gdf11* KO mice exhibiting extended trunk and reduced hindlimb and tail structures[36–40]. We observed that early GDF11

exposure, in combination with FGF2 and CHIR treatment triggered a selective increase in sacral *HOX* gene expression (*HOX*10-13) without affecting expression of anterior *HOX* genes (*HOX*4-9) (Figure 1D). Sacral level *HOX* gene expression did not interfere with NC induction as illustrated by the co-expression of *HOXC9* and *HOXD13* with *SOX10* (Figure 1E) and the expression of *HOXC9* and *HOXD13* in GDF11 treated cultures, enriched by sorting for NC marker CD49D[20] (Figure S1C & D). Based on temporal marker analysis, we outline three distinct stages of sacral NC differentiation (Figure S1E). Immunocytochemical analysis in GDF11 treated cells for co-expression of *SOX10* with *HOXC9, HOXD13* and *Ki67* (Figure S1F& G–I) alongside qRT-PCR analysis (Figure S1J)confirmed sacral NC identity and proliferative state[41]. To validate robustness of the sacral NC protocol, we assessed multiple independent hESC and hiPSC lines for *HOX* gene expression by qRT-PCR and for NC lineage markers via p75NTR and CD49D flow cytometry [20] (Figure S1K&L). Our results demonstrate a robust protocol for the induction of trunk and sacral NC. In combination with work on cranial and vagal NC [19,20,42], our study offers modular access to all four regional NC domains (Figure 1G).

GDF11-mediated expression of 5' *HOX* genes via modulation of RA signaling

The temporospatial sequence of *HOX* gene expression along the AP axis is evolutionarily conserved[43,44]. Co-linearity in *HOX* gene expression from 3' to 5' is maintained in our hPSC platform with 3' *HOX* genes *HOXB4* induced first, followed by *HOXC9* and finally the most 5' *HOX* genes such as*HOXD13* (Figure 2A). Given the key role of GDF11 for enabling expression of the most 5' HOXgenes (Figure 1D), we next assessed GDF11-mediated changes in gene expression and chromatin accessibility during NC differentiation (Figure 2B). Principal component analysis (PCA) of RNAseq and ATACseq data showed time as the main driver of variance (Figure 2C&D). Nevertheless, GDF11 treatment induced a clear segregation within PCA space at D3, D7 and D14 of differentiation. Analysis of *HOX* gene expression confirmed the temporal progression from anterior (3') to posterior (5') *HOX* genes (Figure 2E; S2A). We next integrated RNAseq and ATACseq data to identify candidate genes mediating GDF11 action (Tables S2, S3 and Figure S2B). One class of genes coordinately regulated by GDF11 were GRHL transcription factors, which showed a significant decrease following GDF11 exposure in both gene expression (Figure 2F) and chromatin accessibility (Figure 2G). GRHL factors have been shown to regulate pathways involved in *HOX* gene expression including RA signaling[45,46] and methylation of H3K27[47] and H3K4[48]. During mouse development, RA can cause truncation of tail structures, a phenotype exacerbated in *Gdf11* KO mice and partially rescued by RA inhibition[49]. Interestingly, we observe that direct targets or mediators of RA signaling such as *CRABP2*[50,51] and *CYP26A1*[51] showed reduced expression upon GDF11 treatment (Figure 2H, S2D). Previous work on trunk NC development showed that RA promotes premature EMT and NC induction[52]. Therefore, GDF11 treatment may act by reducing RA signaling and thereby protecting axial progenitors from differentiation and allowing then to reach sacral *HOX* gene levels prior to depletion of progenitor pool (Figure 2I). This hypothesis is supported by increased expression of stem cell-related factors such as *SOX2* and *MYC* (Figure 2J; S2E) in GDF11 treated cultures. To directly test this hypothesis, we assessed how RA signaling affects the patterning of trunk (BMP) versus sacral (BMP + GDF11) NC (Figure 2K). We validated activation of RA signaling and RA inhibition by

AGN exposure by monitoring *CRABP2* expression (Figure 2L). RA promoted expression of anterior *HOX* genes including *HOXB2* and *HOXB6* (Figure 2M S2F) but reduced *HOXC9* expression while RA inhibition resulted in increased *HOXC9* expression (Figure 2N).Importantly, RA inhibition in trunk NC promoted the expression of *HOXC10* (Figure 2O) partially mimicking the effect of GDF11 treatment. Finally, RA activation in GDF11 treated cultures shifted expression towards anterior *HOX* genes and suppressed *HOXC11* and *HOXC13* expression (Figure S2G&H).

Beyond modulating RA signaling, GDF11-mediated induction of sacral HOX genes involves likely additional mechanisms. GO analysis of differentially expressed genes at D3 identified multiple terms related to chromatin regulation (Table S3). We observed increased gene expression for H3K27Me3 demethylases *JMJD6* and *KDM6B* and decreased levels of H3K4 methyltransferases such as *SMYD2* following GDF11 treatment (Figure S2I). These data are consistent with a role of chromatin modification in mediating of GDF11-mediated induction of sacral HOX genes. To test this hypothesis, we performed CUT&RUN experiments for the histone modifications H3K27Me3 and H3K4Me4 at D3 and D14. PCA analysis showed a clear segregation of treatment conditions for H3K37Me3 at D3 and for H3K4Me at D14 (Figure S2J). GDF11 samples showed weaker H3K27Me3 signal at all HOX loci at D4 and stronger H3K4Me3 signal at posterior HOX genes loci (Figure S2K), indicating a faster removal of histone modifications associated with gene repression and gain of modifications associated with gene activation at posterior HOX genes (Figure S2K). Differential H3K27Me3 and H3K4Me3 signals between the BMP and GDF11 conditions are listed in Tables S4.

Sacral NCCs are derived from an NMP-like posterior precursor population

There is clear evidence that NC precursors (D6) can adopt vagal instead of cranial identity following RA exposure[20]. In contrast, the induction of trunk and sacral NC in the current study requires activation of FGF, WNT and GDF11 signaling at much earlier differentiation stages of (D0-3) prior to the emergence of any NC cells. Accordingly, we postulate that trunk and sacral NC are generated not by further caudalizing anterior NC precursors, but by inducing an early, distinct precursor state competent for posterior HOX gene expression. Indeed, by day D3, both trunk and sacral NC protocols gave rise to a SOX2+ precursor population co-expressing *CDX2* and *Brachyury* (*T*) (Figure 3A), markers characteristic of NMPs[53–56]. Gene expression analysis confirmed high *SOX2, T* and *CDX2* levels at D3 (Figure 3B). Flow cytometry showed that around 70% of the cells are SOX2/T/CDX2 triple positive (Figure 3C) and that the proportion of NMPs in the trunk versus sacral protocol is comparable (Figure S3B&C). RNA seq analysis of D3 cells, patterned using either trunk or sacral protocol, showed a strong overlap in gene expression matching the markers previously reported for hPSC-derived NMPs[23] (Figure 3D–F, Table S5). Our data suggest that both trunk and sacral NC induction involve a transient NMP-like progenitor stage followed by the progressive induction of NC markers such as SOX10 and SNAI2 from a CDX2+ precursor population by day 14 and day 20 of differentiation (Figure S3A). However, while many D3 cells were triple positive for SOX2, T, and CDX2, it left the possibility that NC precursors are derived from a minor population of non-NMP cells. To address this concern, we established a dual reporter hPSC line for *SOX2*::H2B-tdTomato; *T*::H2B-GFP

(Figure S3D–H) to purify NMP-like cells at D3 followed by differentiation towards NC lineage (Figure 3G). FACS-purified NMP-like cells (SOX2+/T+ cells) at D3 (Figure 3H; S3I) yielded CD49D+ NC cells at very high efficiencies and with robust co-expression of *SOX10* and *HOXD13* confirming their sacral NC identity (Figure 3I). Therefore, our data demonstrate that hPSC-derived NMP-like cells efficiently contribute to sacral NC lineages and suggest that the induction of trunk and sacral NC involves a distinct precursor and patterning mechanism from that of cranial and vagal NC (Figure 3J).

Sacral NC can be directed to diverse enteric and non-enteric NC fates

Developmental studies in the chick and mouse embryo suggest that sacral NC gives rise to enteric, sympathetic and melanocytic lineages[34,57–60]. To assess whether hPSC-derived sacral NC exhibit similar lineage potential, we established conditions to direct sacral NC differentiation towards each of those lineages (Figure 4A). We isolated purified NC cells via sorting for CD49D, and differentiated them towards enteric neurons in the presence of glial-cell-line derived neurotrophic factor (GDNF) and Ascorbic Acid (AA). By 7 days of differentiation (ENS D30), most sacral NC cells had lost *SOX10* expression and adopted expression of early neuronal marker TUJ1 while maintaining *HOXD13* expression (Figure 4B). At D40, most of the cells had differentiated into neurons while retaining immature morphologies (Figure 4C). At D80, the sacral NC-derived neurons displayed more mature features with complex neuronal morphologies. We observed Tyrosine hydroxylase (TH), GABA (γ-aminobutyric-acid-positive), nitric-oxide-synthase-positive (NOS)+, Choline acetyltransferase (ChAT), and serotonin-positive (5-hydroxytryptamine, 5-HT) neurons (Figure 4D&H) indicating that sacral NC cells generate a broad diversity of enteric neuron subtypes. Gene expression data further confirmed progressive neuronal differentiation by decreased expression of *SOX10* (Figure 4E) and the enteric precursor marker *EDNRB* (Figure 4F). In contrast, *SOX2* expression was retained until D80 (Figure 4G) suggesting the continued presence of neural precursor or immature glial populations during enteric neuron differentiation (Figure S4B). Interestingly, several neuron subtypes such as TH positive neurons showed clustering within distinct domains of the culture dish suggesting derivation from temporally or spatially linked precursors populations (Figure S4A). Those findings are compatible with Edu labeling studies in the mouse in vivo showing that distinct neuron subtypes exit the cycle at different ages [61–63]

To direct differentiation of sacral NC towards sympathetic neurons, CD49D purified cells were treated with high doses of BMP4 and SHH to facilitate differentiation into sympathetic precursors[64]. The resulting precursors were differentiated into sympathetic neurons in the presence of GDNF, AA and Nerve growth factor (NGF) (Figure 4A, **middle**). Interestingly, sympathetic neurons displayed a distinctive morphology and formed extensive fiber bundles projecting radially (Figure 4I; Figure S4C). Most neurons expressed TH and DBH compatible with sympathetic neuron identity (Figure 4I). We also observed expression of *ISL1* under this condition, especially in cells located along neurite bundles emanating from sympathetic neuron clusters (Figure S4D). Sympathetic neuron identity was further confirmed by gene expression analysis (Figure 4J).

To direct melanocytic differentiation, cells were treated with EDN3 at the final stage of sacral NC induction to prime NC lineage towards melanoblast fate and were purified for co-expression of p75NTR and c-Kit at D20. Further differentiation into melanocytes was achieved by using our previously published differentiation protocol[22,65] (Figure 4A, bottom) which resulted in maintenance of *SOX10* expression and melanocytic differentiation via a melanoblast-like intermediate (Figure S4E). Melanocytes were characterized by pigment accumulation and acquisition of more mature melanocyte morphologies (Figure S4F; Figure 4K). Further gene expression analysis confirmed expression of melanocytic makers including *SOX10, hMITF, c-KIT* and pigment related marker: *TYPL1* and *PMEL* (Figure 4L). The successful derivation of sacral NC-derived melanocytes provides access to acral melanocytes, a population of melanocytes located at distal structures such as soles and palms suitable for modeling acral melanoma biology[66].

Vagal and Sacral NC exhibit distinct behavior both *in vitro* and *in vivo*

In quail-chick interspecies studies, it has been shown that vagal and sacral NC exhibit distinct migratory behaviors within the gut[67,68]. However, vagal and sacral ENS lineages are intermingled within the gut making it difficult to isolate and study their specific properties *in vivo*, a challenge particularly pertinent for human studies. Our ability to generate sacral and vagal NC from hPSCs *in vitro* offers the opportunity to directly compare their properties. To this end, we generated vagal NC from a hPSC lines with ubiquitous RFP and sacral NC with ubiquitous GFP expression. In each case AP identity was confirmed through the expression of specific *HOX* genes (Figure 5A&B). We established NC-derived spheroids of either vagal or sacral NC alone or comprised of a 1:1 mixture of both lineages and subjected them to various functional assays *in vitro* and *in vivo*. Vagal NC showed higher propensity for invasion in trans-well invasion assay (Figure 5C) and enhanced migratory capacity in migration and scratch assays (Figure 5D; S5A) compared with sacral NC. An obvious co-culture phenotype was the pronounced self-sorting effect. Although evenly mixed at the start of the experiment (Figure 5E), we noticed that vagal (red) and sacral (green) NC cells segregated under co-culture conditions within just a few days. The same phenotype was observed when switching RFP and GFP cell lines, while no self-sorting occurred when cells of the same NC type were mixed (Figure S5B). We next assessed whether the self-sorting behavior is dependent on cell stage. Vagal and sacral NC spheres, mixed 1:1, were plated and maintained under ENS differentiation conditions for 10 days. Vagal and sacral cells again showed a mutually repellent behavior (Figure 5F, **left panel**). In contrast, dissociation of D10 cells followed by replating and maintenance under ENS conditions for another 20 days were now evenly mixed with no repelling behavior (Figure 5F, **right panel**). These data indicate that the repelling effect is a NC stage-specific feature.

Differences in cadherins and ephrins have been shown to mediate a broad range of cell-cell interactions during development[69–75]. To explore the mechanism underlying the striking repellent behavior observed, we compared RNA seq data from cranial versus vagal NC[20]. We examined both ephrin and cadherin families (Figure 5G; S5D) and found vagal NC and sacral NC exhibited distinct expression patterns. Posterior trunk and sacral NC showed increased *EPHA2, A4, A7* ligand and *EFNA3 and A5 receptor expression*, while anterior cranial and vagal NC show increased *EPHB2, B4* and *EFNB1, B2* expression (Figure 5G).

Vagal and sacral NC shared commonly expressed cadherins, including *CDH1, CDH2* and *CDH3* but also expressed unique sets of cadherins, including *CDH11, CDH18, CDH19, CDH20, CDH23* in sacral and *PCDH1, PCDHB5, PCDHB15* in vagal NC. (Figure S5D).

To compare the functional maturation of enteric neurons derived from vagal versus sacral NC, we performed recordings of electrical activity using a high density multielectrode array (MEA) system. In both groups, electrical activity increased over time in concert with neuronal maturation (Figure S5E). The vagal and sacral-derived enteric neurons show comparable synapse density (Figure 5L; Figure S5F). However, sacral enteric neurons showed a significantly higher spike frequency and increased bursting events when compared to vagal-derived neurons (Figure 5H–K). We further observed that vagal and sacral NC gave rise to different ratios of enteric neurons and glia. For example, vagal NC generated a higher proportion of S100B+ glial progenitors while sacral NC lineages were enriched in NOS+ neurons (Figure S5G). Interestingly, studies in mice indicate the presence of more NOS+ neurons in colon (50%) than small intestine (38%) [76].

Even more striking was the differential *in vivo* behavior of vagal and sacral NC after injection into the cecum of adult NSG mice (carried out in both WT and *Ednrb* KO HSCR model; Figure 6A&B, S6). While sacral NC migrated exclusively towards the distal colon, vagal NC spread both anterograde into the colon and retrograde into the small intestine, with retrograde being the preferred route for vagal NC in the combined sacral/vagal injections (Figure 6C; Figure S6A). Such migratory behavior may reflect a predisposition of each NC lineage to re-populate those regions of the gut normally targeted during early ENS development. Similar mixing experiments carried out in *Ednrb* KO mice, confirmed the presence of both vagal (RFP) and sacral (GFP) in various sections of the gut but yielded higher proportions of vagal cells in the small intestine (Figure 6D, **upper**) versus increased proportions of sacral cells in the distal colon (Figure 6D, **bottom**). A subset of those cells projected toward villi structures (Figure S6B) and differentiated into ENS neuron subtypes such as CHAT and NOS (Figure S6C).

Combined vagal and sacral NC for treating HSCR mouse model of total aganglionosis

Mutations of *EDNRB* are among the most common genetic alterations in HSCR. For the current study, we used the B6.129S7-*Ednrb*^{tm1Ywa}/FrykJ mouse, in which Exon 3 of the *Ednrb* gene is replaced by a neomycin resistance cassette. This mouse exhibits extensive aganglionosis and suffers from a megacolon phenotype. To allow for xenografting studies, we crossed *Ednrb* KO with NSG mice (NOD.Cg-*Prkdc*^{scid} *Il2rg*^{tm1Wjl}/SzJ) for 10 generations. The lack of enteric neurons in KO mice was confirmed by staining with TUJ1 and H&E staining (Figure 7A; S7B). Interestingly, *Ednrb* KO mice on the NSG background showed a very severe megacolon phenotype with all the animals dying between D28-D30 (Figure S7A). In contrast, *Ednrb* KO mice on a B6.129S7 background showed broader survival rates (D28-D50; Figure 7B). In the *Ednrb* KO / NSG mice, the aganglionosis extended beyond the colon into the small intestine, which may explain the severity of the HSCR phenotype (Figure S7D). Those mice also exhibited a much thinner gut wall and impaired villi structure compared to age-matched WT NSG mice (Figure 7C&D, Figure

7C). Therefore, we used *Ednrb* KO / NSG mice as a model of total aganglionosis and tested the potential of hPSC-derived NC lineages for rescuing the most severe form of HSCR.

Ednrb KO mice (2 weeks of age) were injected at the level of the caecum with either vagal, sacral, or a 1:1 mix of vagal and sacral NC cells, or with Matrigel (control) only (Figure S6A). All control mice (Matrigel only) died within a month after birth and displayed a megacolon phenotype at autopsy. Mice injected with sacral NC failed to show any rescue effect. Mice injected with vagal NC showed a small increase in life span, but none of the mice survived past D40. In contrast, a subset of the mice injected with a 1:1 mixture of vagal and sacral NC showed clear improvements in survival time beyond one month with a maximal lifespan in excess of 9 months, referred to as “rescued mice” (Figure 7E). While untreated HSCR mice displayed an extremely thin gut wall, this phenotype was partially rescued in the combined vagal + sacral NC grafted animals (Figure 7F&G, Figure S7F). We also observed a progressive gain in body weight in rescued mice although at slower rate compared with their healthy siblings (Figure 7H).

To confirm the restoration of gut motility, we performed video imaging of colonic migration motor complexes (CMMCs) in rescued mice. CMMCs were observed in 9 months old KO mice that had received transplantation of vagal + sacral NCCs, which clearly demonstrated that rescued mice showed restored gut motility (Figure 7K; Figure S7G). However, rescued mice showed a higher frequency and velocity of CMMCs compared with age-matched WT mice (Figure 7L). The colon width of rescued mice at proximal colon and distal colon was comparable with WT but showed a higher width at mid-colon region (Figure 7M). Interestingly, data of gastric emptying and small intestine transit showed no difference between WT and rescued mice (Figure 6I&J). Finally, we performed whole mount staining of the gut portion with restored function to determine the structure and composition of neuronal networks. We confirmed the presence of graft-derived vagal (RFP) and sacral (GFP) neurons ($TUJ1^{+}$) in different regions of the gut and, most notably, the formation of neuronal networks in the aganglionic segments (Figure 7N). We further observed the presence of some human-derived non-neuronal lineages (Figure 7Q), which might reflect glial cells or immature precursors based on morphology. Our data demonstrates that combined PSC-derived vagal + sacral NC injections can rescue a very severe HSCR mouse model with aganglionosis in both the large and small intestine (Figure 7R), a model which was not rescued by transplantation with either vagal or sacral NC cells alone.

DISCUSSION

A human PSC-based platform for all major NC populations along the AP axis

Our study offers access to all major human NC lineages including cranial, vagal, trunk and sacral NC. While there is evidence for considerable NC fate plasticity based on quail-chick chimera studies[77–80], previous work from our group (including current study) and from others[79,81–85] indicate that hPSC-derived NC cells of distinct axial identities exhibit biased lineage potential. The derivation of some NC lineages such as sympathetic or enteric neurons is restricted to specific NC domains such as trunk and sacral NC while other cell types such as melanocytes can be derived from NC cells at all AP levels[86]. It remains unclear what drives distinct differentiation potential across NC domains, but our

hPSC-based data suggest intrinsic factors govern their differential behavior under identical *in vitro* conditions. The NC protocols presented here should provide a powerful platform for studying NC development and disease and for applications in regenerative medicine.

HOX gene expression and the sequential generation of NC cells

We report that FGF and WNT signaling promotes the expression of posterior *HOX* genes without impacting NC differentiation potential. However, we observe a delay in NC induction in response to increasing levels of FGF and WNT signaling, (Figure S1M), reminiscent of the delay in sacral NC migration observed *in vivo*[87]. Such delayed induction *in vitro* may reflect the spatiotemporal sequence of generating NC domains along the AP axis *in vivo*, starting at cranial and vagal levels before progressing sequentially to trunk or sacral levels. Given the well-known role of WNT and FGF signaling in promoting precursor cell proliferation and maintenance of stem cell-like states, it seems plausible that prolonged periods of precursor cell identity may facilitate the sequential progression of *HOX* gene expression from anterior 3' to posterior 5' genes. A similar effect of FGF and WNT signaling on AP identity has been previously reported for the development of limb[88] and the generation of presomitic mesoderm[25].

Axial progenitors and the role of GDF11 in sacral level *HOX* gene induction.

A critical step in deriving sacral NC was the identification of GDF11 as a factor driving the transition from trunk to sacral identity. However, the mechanism by which GDF11 exerts this function remains poorly understood. We report decreased expression of GRHL transcription factors and a sustained, negative regulation of RA signaling by transient GDF11 treatment, and we could partially mimic the effect of GDF11 by inhibiting RA signaling. Studies in the mouse suggest that axial progenitor proliferation is dependent on LIN28A while GDF11 controls the balance between proliferation and differentiation via regulation of *HOX13* genes[89]. Another study shows that LIN28A/let-7 pathway regulates *HOX* expression via polycomb-related genes[90]. Both studies reported an inhibitory relationship between *LIN28A* and *HOX13* similar to that we observed in our current data set.

Our data indicate that SOX2/ T double positive NMPs give rise to posterior NC lineages including trunk and sacral NC. NMPs can contribute to spinal cord and paraxial mesoderm lineages *in vitro*[26–28,91] and *in vivo*[25,26,54,92–96]. The contribution of hPSC-derived NMPs to NC development has been previously reported for trunk NC lineages[23]. A key unresolved question is whether our *in vitro* data reflect an *in vivo* requirement for an NMP-intermediate during trunk NC development. A recent study in zebrafish integrated single cell epigenomics and transcriptomics data of NMPs and NC cells to conclude that at least a portion of the posterior NC in zebrafish is derived from NMPs[24]. It will be critical to address this question in additional model organisms.

Difference between vagal and sacral NC-derived enteric neural lineages

The direct comparison of vagal and sacral NC lineages revealed differences in migratory behavior, relative proportion of neuronal and glial subtypes and neuronal activity. Further studies will be required to determine the mechanisms driving differential migration

behavior such as the role of differentially expressed surface markers (Figure 5G; S5D) or differential responses to extrinsic factors present in small versus large intestine, such as GDNF and EDN3 (Figure S5C). Studies of chick development indicate that colonization of colorectal region by the enteric NCCs is a complex process. Vagal NCCs initially migrate within the submucosa, then move towards the myenteric plexus, while sacral NCCs are initially located primarily in the myenteric plexus and subsequently migrate towards the submucosal region[67]. Local repelling effects may contribute to those distinct migratory pathways. The repellent effects observed in our study could be a manifestation of developmental mechanisms guiding vagal versus sacral NCCs but being accentuated by the high number of vagal and sacral cells interacting at the injection site. Moreover, host tissue microenvironment, graft location and development stage of the transplanted cells may also be important factors. Finally, it would be interesting to purify or select specific neuronal subtypes from either vagal and sacral NC to address whether there are intrinsic differences for each neuronal subtype or whether functional differences between sacral and vagal NC are due to differences in relative subtype composition. Access to defined neuronal subtypes will be relevant for applications in disease modeling and regenerative medicine beyond HSCR, such as the use of NOS+ neurons for the potential treatment of diabetic neuropathy.

A role of sacral NC in stem cell-based cell therapy for HSCR

There has been considerable interest in developing cell-based therapies for the treatment of HSCR and other ENS disorders[9]. Our past work[20] provided proof-of-concept for the use of hPSC-derived NC in preclinical HSCR models. Advantages of hPSC-derived ENS precursors include scalability, and access to the earliest stages of ENS development, when cells are capable of extensive *in vivo* migration[97]. While grafting sacral NC alone could not rescue the severe *Ednrb* KO model, we demonstrate long-term in vivo engraftment in wt x NSG mice giving rise to neuronal cells (Figure S6D), and non-neuronal cells (Figure S6H), of which some are perhaps glial-like cells based on the morphology. A key result was requirement for combined vagal and sacral NC injections to rescue a total aganglionosis model of HSCR. While future studies are required to address the mechanisms underlying this requirement, it is possible that the self-sorting behavior of the two lineages may promote a more rapid and widespread migration of each NC lineage *in vivo*. Given the prominent small intestine phenotype in our Ednrb KO model, robust re-population of the small intestine by vagal NC cells in combined grafts may mediate enhanced survival by improving small intestine function including food absorption and barrier function. If enhanced migration and repopulation of the small intestine is key, this requirement may be bypassed in humans by performing multiple injections along the small intestine, a strategy not feasible in the much smaller mouse gut. If the rescue depends on the unique combination of cell types present in combined sacral and vagal grafts, it will be important to include both populations for future translation. In either case, the ability to rescue a mouse model of total aganglionosis indicates considerable therapeutic potential in patients with severe HSCR.

Limitations of the study

A limitation of our study is that we injected cells only at the NC stage, based on their predicted migration ability, while no later stage cells were tested. Similarly, more studies are needed to define optimal injection sites, cell numbers, cell composition and other parameters

critical for eventual translation. Second, we used a mouse model representing a very severe form of HSCR, which leaves a very narrow time window for surgery and for the transplanted NC cells to migrate and trigger recovery in the host tissue. Therefore, it will be important to assess the effect of combined vagal / sacral grafts in milder models of HSCR, and to assess their relative contribution to recovery. Third, due to current technical limitations, all the functional studies were end-point assays, which prevented us from defining predictable criteria for long survival at earlier stages post transplantation. Novel assays that enable real-time assessment of the transplanted cells are required. Finally, while we demonstrate functional rescue including restoration of gut motility, we do not yet understand the relative contribution of various mechanisms to the overall rescue in survival, such as the impact of the grafted cells on barrier function, maintenance of gut wall thickness, gut motility or food absorption.

STAR METHODS

RESOURCE AVAILABILITY

Lead contact—Further information and requests for resources and reagents should be directed to and will be fulfilled by the lead contact, Lorenz Studer (studerl@mskcc.org).

Materials availability—The *SOX2*::Tomato/*T*::GFP dual reporter line is available for distribution through the SKI stem cell research facility via MTA. The study did not generate other unique reagents.

Data and code availability—RNA-seq (GSE199439), ATAC-seq (GSE199440) and CUT&RUN (GSE199441) data have been deposited at GEO and are publicly available as of the date of publication. Microscopy data reported in this paper will be shared by the lead contact upon request. This paper does not report original code.

Any additional information required to reanalyze the data reported in this paper is available from the lead contact upon request.

EXPERIMENTAL MODEL AND SUBJECT DETAILS.

Human cell lines—Experiments are largely carried out using the human embryonic stem cell (hESC) line H9 (WA-09) or reporter lines derived from H9 (WA-09). The human embryonic stem cell (hESC) lines H1 (WA-01), HUES6 and MEL1 were also used to repeat the experimental results generated with H9. Human induced pluripotent stem cell (iPSCs) lines 348.7, 706.3 and 864.3 (previously published in[98 99] were also used to repeat critical experiments.

Reporter lines used in this study are as follows: The H9-derived *SOX10*::GFP reporter line was generated as reported previously[16]. The H9-derived GFP and mCherry lines were generated by lentiviral infection. The H9 and H1-derived *SOX2*::Tomato/*T*::GFP dual reporter lines were generated through a CRISPR knock-in method, which was validated by PCR and sequencing. All cell lines used were karyotypically normal as assessed by G-banded chromosomal analysis. All modified cell lines used were generated by the MSKCC Stem Cell Core as described in the methods section below.

All cell lines are authorized to use under the supervision of Tri-SCI ESCRO Committee. The culture conditions are described below in method details.

Animals—All experimental procedures involving mice were done in accordance with approved protocols by the Institutional Animal Care and Use Committee (IACUC) and Research Animal Resource Center (RARC) at Memorial Sloan Kettering Cancer Center (MSKCC), and the mice were handled in accordance with the principles and procedures of the Guide for the Care and Use of Laboratory Animals under the approved protocol 18-01-001. All mouse strains were maintained on a predominantly NSG background. Genotyping is performed by Transnetyx. Animals were weaned 21 to 28 days after birth and handled and euthanized according to procedures approved by RARC of MSKCC. Mice of both sexes were used in all experiments, and they were either randomly assigned to the experimental groups or used with littermate controls. Mouse strains used in this study are NSG (NOD.Cg-Prkdcscid Il2rgtm1Wjl/SzJ) mice and an NSG derived disease model line carrying the *Ednrb* ^{tm1Ywa}/FrykJ mutation[8,100].

METHOD DETAILS

Culture of hESC and iPSC in Essential (E8) medium—hESC or iPSC were plated on 10 cm dishes coated with Vitronectin (1:100 diluted in DPBS and coated in cold room overnight) and maintained in E8 medium (Thermo Fisher, A1517001). The E8 medium was changed every day and the cells were passaged every 3-5 days at 70-85% confluence. The cells were passaged using EDTA dissociation (0.5 mM EDTA + 1.8g/l (30.8 mM) NaCl (Sigma-Aldrich) in DPBS) at 1:15 ratio as described previously[99].

NC differentiation—The basic NC differentiation protocols used in this study are based on previous work[19,20]. Briefly, matrigel (Thermo Fisher, A1413201) was diluted at 1:100 ratio in DMEMF-12 (Thermo Fisher, 21331020) and plates were coated with the diluted matrigel overnight at 4°C. For inducing differentiation, hESCs or iPSCs were dissociated at 70%-80% confluence using EDTA dissociation buffer and replated as a single cell suspension on matrigel-coated 24-well plates at a density of 100K cells/cm^2 in E6 medium containing 10 μM ROCK-inhibitor (Y-27632; R&D, 1254). The cells were kept in E6 medium (Thermo Fisher, A1516401) + Y-27632 overnight. The next day, the medium was switched to NC induction medium. For cranial differentiation, the cells were kept in E6 medium containing 10 μM SB431542 (R&D, 1614), 1ng/ BMP4 (R&D, 314-BP), and 0.6μM CHIR (R&D, 4423) for the first 2 days and then switched to E6 medium containing 10 μM SB431542 and 1.5μM CHIR for 10 days. For vagal NC the same conditions were used with an additional 1μM RA (Sigma, R2625) added to the medium starting from D6. To establish the sacral NC protocol, the cranial NC protocol was modified with varying concentrations of FGF2 (R&D, 233-FB/CF), CHIR and GDF11 (Peprotech, 120-11), added at different time points as detailed in the results section. For the generation of melanocytes, 100nM EDN3 (American Peptide company, 88-5-10B) was added to the sacral NC protocol from day 14 to day 20. In experiments testing the RA hypothesis, the sacral NC protocol was modified using either 1μM RA (Sigma, R2625) or 100nM AGN (Tocris, 5758) as detailed in the experimental design section.

RNA extraction and RT-qPCR—RNA was prepared from samples collected with the Zymo Direct-zol Kit and extracted using the Direct-zol RNA MiniPrep kit. cDNA was generated using the iScript Reverse Transcription Supermix for RT-qPCR. For qPCR analysis, primers were obtained from QIAGEN (Quantitect Primer assays, see key resources table and Table S1 for details) or IDT and the reactions were performed following manufacturers' instructions using SsoFast EvaGreen® Supermix. The Assays were run on Bio-Rad CFX384 Real-Time PCR machine. Results were normalized to GAPDH housekeeping genes.

Immunostaining for cultured cells—Cultured cells were fixed with 4% PFA for 10-20 minutes, then blocked and permeabilized in IF buffer (PBS + 1% BSA + 0.3% Triton X-100). Primary antibodies were diluted according to the manufacturer's recommendation in IF buffer + 5% normal donkey serum or 5% normal goat serum. The fixed cells were incubated with primary antibody overnight at 4°C. Primary antibody was washed with PBS+0.01% Tween-20 (PBS-T) for 10 minutes, repeated 3 times. Cells were then incubated in secondary antibody conjugated with Alexa Fluor 488- 555-, or 647- diluted at 1:500 in IF buffer + 5% normal donkey serum or 5% normal goat serum for 1 hour at room temperature. The secondary antibody was also washed with PBS-T 3 times, 10 minutes each time. Between the second wash and third wash, cells were stained with 4′, 6-diamidino-2-phenylindole (DAPI) for 10 minutes.

Flow cytometry—Cells were disassociated with Accutase for 20-40 minutes depending on cell types at 37 °C. After neutralizing with DMEMF-12 containing 2% FBS and washing once with DMEMF-12, cells were filtered with 40μm filter. If the cells were derived with reporter lines, the cells were resuspended in DMEMF-12 containing 2% FBS and 10μM DAPI and sorted or analyzed directly by BD LSRFortessa™ or BD FACSAria™. If the cells needed to stain for cell surface markers, the cells were resuspended in DMEMF-12 containing 2% FBS and diluted primary antibodies following manufacturers' instruction and incubated on ice for 30 minutes. The cells were washed with DMEMF-12 twice and then resuspended in DMEMF-12 containing 2% FBS and 10μM DAPI for sorting or analysis. If the cells needed to be stained for intracellular markers, the cells were resuspended 1× PBS with 2 μg/ propidium iodide to determine the live or dead population. Then the cells were washed with PBS, then fixed and permeabilized using BD Cytofix/Cytoperm (BD Bioscience, 554722) on ice for 30 min. Fixed cells were then permeabilized and stained using 1× BD Perm/Wash Buffer (BD Bioscience, 554723) following the manufacturer's instructions. Results were analyzed using FlowJo.

RNA sequencing (RNA-seq)—Cells were disassociated with Accutase for 20 minutes at 37 °C. The cells were collected into 15mL falcon tubes and DMEMF-12 containing 2% FBS was added to neutralize the enzyme. The cells were spun down and washed with PBS twice. The cells were spun down again in 1.5mL Eppendorf tube and resuspended in 500μL TRIzol (ThermoFisher catalog # 15596018) and stored at −80°C. When all data points were collected, the samples underwent RNA extraction and RNA-seq as performed by the IGO core at MSKCC.

Briefly, phase separation in cells lysed in 1mL TRIzol Reagent was induced with 200μL chloroform and RNA was extracted from the aqueous phase using the miRNeasy Mini Kit (Qiagen catalog # 217004) on the QIAcube Connect (Qiagen) according to the manufacturer's protocol with 350μL input. Samples were eluted in 15μL RNase-free water. After RiboGreen quantification and quality control by Agilent BioAnalyzer, 500ng of total RNA with RIN values of 9.6-10 underwent polyA selection and TruSeq library preparation according to instructions provided by Illumina (TruSeq Stranded mRNA LT Kit, catalog # RS-122-2102), with 8 cycles of PCR. Samples were barcoded and run on a HiSeq 4000 in a PE100 run, using the HiSeq 3000/4000 SBS Kit (Illumina). An average of 53 million paired reads was generated per sample and the percent of mRNA bases averaged 85%.

RNA-seq bioinformatics—STAR aligner[101] was used to map reads to the human genome (GRCh37). The 2-pass mapping method[102] was used, in which the reads are mapped twice. SAM files were processed and converted to BAM format using PICARD tools and then HTseq was used to compute the expression count matrix from the mapped reads. DESeq2[103] was used to normalize the raw counts (Median of Ratios method) and perform differential gene expression analysis. Data are presented on a gene-by-gene basis as normalized counts or after carrying out a variance-stabilizing transformation followed by PCA analysis.

ATAC sequencing (ATAC-seq)—Cells were disassociated with Accutase for 20 minutes at 37 °C. The cells were collected into 15mL falcon tubes and DMEMF-12 containing 2% FBS was added to neutralize the enzyme. The cells were spun down and washed with PBS twice. The cells were spun again in a 1.5mL Eppendorf tube and resuspended in 500μL stem cell banker cell freezing buffer and stored at liquid nitrogen tank. When all data points were collected, the samples were sent to IGO core. ATAC-seq was performed by IGO core at MSKCC.

Profiling of chromatin was performed by ATAC-Seq as described in[104]. Briefly, 50,000 viably frozen neural crest cells were washed in cold PBS and lysed. The transposition reaction was carried out using TDE1 Tagment DNA Enzyme (Illumina catalog # 20034198) incubated at 37°C for 30 minutes. The DNA was cleaned with the MinElute PCR Purification Kit (QIAGEN catalog # 28004) and material was amplified for 5 cycles using NEBNext High-Fidelity 2X PCR Master Mix (New England Biolabs catalog# M0541L). After evaluation by real-time PCR, 7-10 additional PCR cycles were done. The final product was cleaned by aMPure XP beads (Beckman Coulter catalog # A63882) at a 1X ratio, and size selection was performed at a 0.5X ratio. Libraries were sequenced on a HiSeq 4000 in a PE100 run, using the HiSeq 3000/4000 SBS Kit (Illumina). An average of 42 million paired reads were generated per sample. Transposition of native chromatin for fast and sensitive epigenomic profiling of open chromatin, DNA-binding proteins, and nucleosome position.

ATAC-seq bioinformatics—ATAC-seq data was processed following the recommendations of the ENCODE consortium (The ENCODE Consortium ATAC-seq Data Standards and Prototype Processing Pipeline https://www.encodeproject.org/atac-seq/). Reads were aligned to the human reference genome (GRCh37) with BWA-backtrack[105]. Post-alignment filtering was done with samtools[106] and Picard tools[107] to remove unmapped reads, improperly paired reads, non-unique reads, and duplicates. To identify

regions of open chromatin represented by enrichments of reads, peaks were called with MACS2[108]. Peaks with an adjusted P < 0.01 were merged, quantified, and normalized using DiffBind v3.2.1[109]. ATAC-seq signal profiles were created with bamCoverage from the deepTools suite[110] using the following parameters: -bs 10 --normalizeUsing RPGC --effectiveGenomeSize 2776919808 --blackListFileName hg19-blacklist.v2.bed --ignoreForNormalization chrX chrY --ignoreDuplicates --minFragmentLength 40. Blacklisted regions[111] were retrieved from https://sites.google.com/site/anshulkundaje/projects/blacklists.

Generation and validation of H9 *SOX2*::tdTomato/*T*::GFP dual reporter line— H9 *SOX2*::tdTomato/*T*::GFP dual reporter lines were generated using CRISPR/Cas9 based HDR method [112]. Briefly, the sgRNA were designed to target a sequence close to the stop codon of the *SOX2* or *T* gene. Each target sequence was cloned into the pX330-U6-Chimeric_BB-CBh-hSpCas9 vector (Addgene plasmid #42230) to make the gene targeting constructs. For *SOX2* targeting, a donor plasmid containing a 400 bp left homology arm, followed by a P2A-H2B-tdTomato cassette, and a 400 bp right homology arm was used as the template for HDR. The sgRNA and the donor plasmid were electroporated into H9 cells using a Lonza 4D-Nucleofector instrument with Solution “Primary Cell P3”, and Pulse Code “CB-150”. 4 days after electroporation, tdTomato+ cells were sorted out and expanded. Single-cell clones were then isolated, and the following PCR and Sanger sequencing were used to verify knock-in. The *T*::GFP reporter cells were generated on top of the validated *SOX2*::tdTomato cells. For *T* targeting, a donor plasmid containing a 400 bp left homology arm, followed by a P2A-H2B-GFP cassette, a floxed puromycin selection cassette (loxP-PGK-puro-loxP) and a 400 bp right homology arm was used as the template for HDR. The sgRNA and the donor plasmid were electroporated in to H9 *SOX2*::tdTomato cells. 0.5 μg/mL Puromycin was added to the 3 days post-electroporation for 4 days. Single-cell clones were generated, PCR and Sanger-sequencing were used to identify correctly knock-in clones. The dual reporter cells expressed *SOX2*-tdTamato at the hESC stage, and expressed *T*::GFP in hESC-derived mesoendoderm stage, which performed using a 1-day mesoendoderm differentiation protocol [112]. The dual reporter showed a normal karyotyping (G-banding).

The sg RNA and primers used were listed in Table S1_Primers.

Generation of lentivirus based H9::mCherry and H9::GFP cyto-reporter line.— The Lentiviral vectors: PLVX-EF1a-mcherry and PLVX-EF1a-GFP were purchased from Takara. The Lenti-virus were made in HEK293T cells with packaging plasmid: psPAX (Addgene: 12260), and envelope plasmid pMD2.G (Addgene 12259). H9 cells were infected with the lentivirus. The mCherry or GFP expression cells were sorted at day 4 post-infection and expanded. Fluorescent images showed the H9::mCherry or H9::GFP constitutively express mCherry or GFP, respectively . The cells maintained as normal karyotype.

Enteric neuron differentiation—*In vitro* differentiation of NC to enteric neurons was carried out as previously described[20]. Briefly, the vagal NC or sacral NC cells were purified by FACS by the cell surface marker CD49D. The purified NC were then cultured in neural spheroid medium for 4 days in ultra-low attachment plates. Neural spheroid

medium is comprised of neurobasal (NB) medium supplemented with I-glutamine (Gibco, 25030-164), N2 (Stem Cell Technologies, 07156), B27 (Life Technologies, 17504044) and NEAA, CHIR99021 (3μM, Tocris Bioscience, 4423) and FGF2 (10nM, R&D Systems, 233-FB-001MG/CF). The aggregated NC spheroids were plated on polyornithine/laminin/fibronectin (PO/LM/FN)-coated plates. The method PO/LM/FN coated plates preparation has be previously described[42]. Then the cells were switched to enteric neuron differentiation medium, containing neurobasal (NB) medium supplemented with l-glutamine (Gibco, 25030-164), N2 (Stem Cell Technologies, 07156), B27 (Life Technologies, 17504044) and NEAA, containing GDNF (25ngmL–1, Peprotech, 450-10) and ascorbic acid (200μM, Sigma, 4034-100g). The cells were fixed for immunostaining or collected for gene expression analysis at different days of differentiation.

Sympathetic neuron differentiation—*In vitro* differentiation of NC to sympathetic neurons was carried out as described[23]. Briefly, the sacral NC cells were purified using FACS on the basis of the cell surface marker CD49D. The purified NC were then cultured in neural spheroid medium for 4 days in ultra-low attachment plates. The aggregated NC spheroids were plated on poly-ornithine/laminin/fibronectin (PO/LM/FN)-coated plates. The cells were then cultured in a medium containing high BMP4 and SHH for 4 days. This medium consisted of neurobasal (NB) medium supplemented with I-glutamine (Gibco, 25030-164), N2 (Stem Cell Technologies, 07156), B27 (Life Technologies, 17504044), NEAA, BMP4 (50ng/mL , R&D, 314-BP) and recombinant SHH (C25II) (50ng/mL, R&D, 464-SH). Following this, the cells were switched to sympathetic neuron differentiation medium, containing neurobasal (NB) medium supplemented with l-glutamine (Gibco, 25030-164), N2 (Stem Cell Technologies, 07156), B27 (Life Technologies, 17504044), NEAA, ascorbic acid (200μM, Sigma, 4034-100g), NGF (10ng/mL, Peprotech, 450-01), BDNF (10ng/mL, R&D, 248-BDB) and GDNF (10ng/mL, Peprotech, 450-10). The cells were fixed for immunostaining or collected for gene expression analysis at different days of differentiation.

Melanocyte differentiation—EDN3 (100nM, American Peptide company, 88-5-10B) and BMP4 (5ng/ml, R&D, 314-BP) was added from day 14 to day 20 on top of the sacral neural crest differentiation. At D20, the cells were purified by FACS by P75NTR and cKIT cell surface marker, and double positive population were sorted out. The sorted melanoblasts were plated onto dried PO/LM/FN dishes as droplets. After 30 minutes, melanocyte medium was slowly added to the plate. The melanocyte medium contains neurobasal (NB) medium supplemented with l-glutamine (Gibco, 25030-164), N2 (Stem Cell Technologies, 07156), B27 (Life Technologies, 17504044) and NEAA, SCF (50ng/mL, R&D, 255-SC-MTO), CAMP (500 μM, Sigma, D0627), FGF2 (10ng/mL, R&D, 233-FB/CF), CHIR (3 μM, R&D, 4423), BMP (25ng/mL, R&D, 314-BP), EDN3 (100nM, American Peptide company, 88-5-10B). The cells are fed every 2-3 days and passaged when the cells reach 70-80% of confluency, using Accutase for 20min at 37 C for cell detachment. The cells were fixed for immunostaining or collected for gene expression analysis at different days of differentiation.

Immunostaining of tissue sections—The gut tissue collected from mouse was cleaned with cold PBS using a syringe with a pipette tip stuck to the end. The gut tubes were then

opened using scissors and flatted as a sheet. The flatted gut tubes were rolled up ("Swiss Roll" technique) and were fixed with 4% PFA overnight at 4°C. They were then washed 3 times with PBS and transferred to 70% ethanol for Paraffin embedding. The paraffin embedding, slide preparation and Hematoxylin and Eosin (H&E) staining were performed by the Sloan Kettering Institute, Molecular Cytology Core. For immunofluorescent staining, the slides were brought to room temperature for 1 hour before staining. We used the Trilogy kit (Cat#920P-07) from Cell Marque and followed the protocols from the manufacturer for antigen retrieval. In brief, the slides were placed in Trilogy buffer and subjected to high pressure and temperature using an Electric Pressure Cooker set to "high" for 15 minutes. The slides were rinsed in clean hot Trilogy buffer for 5 minutes and washed 3 times in PBS. The slides were then processed following the normal immunostaining protocol as described above for cultured cells before being sealed with anti-fade medium and cover glass prior to imaging.

Whole-mount dissections and Immunostaining of gut tissue from grafted mice

—Freshly dissected distal ileum (3cm) and full-length colon were placed on a sylgard-coated petri dish and cut open along the mesenteric border to reveal the mucosal surface. Flat laminar preparations, mucosal-side up, were obtained by stretching and pinning out the tissue prior to fixation with 4% PFA overnight at 4°C. After washing three times with PBS, tissues were micro-dissected to remove the mucosa from the submucosal plexus (SMP) and the underlying circular muscle, to obtain preparations of longitudinal muscle-myenteric plexus (LMMP). Both SMP and LMMP preparations were incubated in 1% Triton X-100 in PBS for 30-45 minutes at room temperature followed by three washes with PBS prior to incubation with primary antibodies for 48-72 hours at 4°C. Following incubation with primary antibodies, tissues were incubated with secondary antibodies as described above for two hours at room temperature. Preparations were then washed with PBS and mounted on a glass slide using DAKO fluorescent mounting media (Agilent Technologies).

Migration and co-differentiation assays

Transwell assay: To test capacity of NC cells for invasion, we used the CytoSelect 24-Well Cell Invasion Assay, Basement (Cell Biolabs). We plated 200K cells per chamber in neural spheroids medium and added 500μL of neural spheroid medium containing 10% fetal bovine serum to the lower well of the invasion plate and incubated the plate for 48h at 37°C in 5% CO2 atmosphere. Cells that crossed through the invasion chamber were stained with the Cell Stain Solution, provided with the kit (Cell Biolabs), and examined under the microscope. The stained cells were then lysed and measured by plate reader for quantification.

Migration assay: Vagal or sacral neural spheroids were generated as described in enteric neuron differentiation section. Those spheroids were plated down on a 2D PO/LM/FN coated plated for assessing surface migration or embedded in 3D Matrigel for assessing migration within a Matrigel pellet. Pictures were taken at sequential time points post plating to trace the migration process.

Scratch assay: Vagal or sacral NC cells were plated on PO/LM/FN coated 24 well plates at density of 100 x 10^3 cells per cm^2. After 24 h, the culture lawn is scratched manually using a

pipette tip. Live images are taken at different time points after the scratch was made to trace the migration.

Transplantation of NC in adult colon—The procedure for colon transplantation has been previously described[20].

All mouse procedures were performed following NIH guidelines and were approved by the local Institutional Animal Care and Use Committee (IACUC), the Institutional Biosafety Committee (IBC) as well as the Embryonic Stem Cell Research Committee (ESCRO).

We used 4–6 weeks old male NSG (NOD.Cg-Prkdcscid Il2rgtm1Wjl/SzJ) mice or 2-3 weeks old *Ednrb* KO/NSG homozygous mice for these studies. Animal numbers were based on availability of homozygous hosts and on sufficient statistical power to detect large effects between treatment versus control as well as for demonstrating robustness of migration behavior (NSG). Animals were randomly selected for the various treatment models but assuring for equal distribution of male/female ratio in each group. All *in vivo* experiments were performed in a blinded manner. Animals were anaesthetized with isoflurane (1%) throughout the procedure. A small abdominal incision was made, abdominal wall musculature lifted, and the caecum is exposed and exteriorized. Warm saline was used to keep the caecum moist. Then 20μL of cell suspension (2–4 million GFP+ or RFP+ CD49D-purified human ES-cell-derived NC cells) in 70% Matrigel (BD Biosciences, 354234)/PBS or 20 μL of 70% Matrigel in PBS only (control-grafted animals) was slowly injected into the caecum (targeting the muscle layer) using a 27-gauge needle. Use of 70% matrigel as carrier for cell injection assured that the cells stayed in place after the injection and prevented backflow into the peritoneum. After injection that needle was withdrawn, and a Q-tip was placed over the injection site for 30s to prevent bleeding. The caecum was returned to the abdominal cavity and the abdominal wall was closed using 4-0 vicryl and a taper needle in an interrupted suture pattern and the skin was closed using sterile wound clips. After wound closure animals were put on paper on top of their bedding and attended until conscious and preferably eating and drinking. The tissue was collected at different time points (ranging from two weeks to 9 months) after transplantation for histological analysis.

Intestinal Motility—Motility of stomach, small intestine, colon were evaluated as previously described [113]

Gastric Emptying and Small Intestinal Transit: 9-month-old Mice were orally gavaged rhodamine B dextran (100mL, 10mg/mL in 2% methylcellulose; Invitrogen, Waltham, MA) using a 21-gauge feeding needle. 15 minutes after gavage, mice were euthanized, and their stomach and small intestine were removed and the small intestine was divided into 10 segments. The stomach and all segments of the small intestine were then placed in 0.9% NaCl, homogenized and centrifuged (2000 g). One ml of the supernatant was extracted for measurement of fluorescence using a fluorescent plate reader (BioTek Synergy Neo2, Winooski, VT). Rhodamine B dextran (1:400 dilution) and 0.9% NaCl were used as positive and negative controls, respectively. Gastric emptying was calculated as the fluorescence of the stomach over the total fluorescence of the stomach plus the 10 sections of small intestine. For small intestinal transit, the fluorescence of each small intestinal segment was

first evaluated as a proportion of the total fluorescence. The sum of all 10 segments was then obtained as the final geometric center measurement of each animal[113,114].

Video imaging of Colonic Migrating Motor Complexes: To evaluate ex vivo colonic motility for ENS-driven peristaltic contractions, the entire colon of each mouse was extracted and immediately placed in an organ bath under physiologic conditions where it continuously superfused with carbogenated (95% O2; 5% CO2) Krebs solution at 33-37°C. Each colon was cannulated at both the proximal and distal ends to maintain consistent intraluminal front and back pressure, respectively. After cannulation, colons were equilibrated for 30 minutes in the organ bath before baseline measurements were obtained for one hour. Colonic contractions were visualized using a Logitech Quickcam pro camera (Newark, CA) positioned above the organ bath. 15-minute video recordings were obtained throughout the experiment which were then converted into spatiotemporal heat maps using an edge-detection software[113–116]. Spatiotemporal maps were then visualized using the MATLAB R2014a software with a custom-written Analyse2 plugin.

Multi-electrode array recording (MEA assay)—hPSC-derived vagal NC or sacral NC were seeded onto poly-l-lysine-coated complementary metal oxide semiconductor multi-electrode arrays (CMOS-MEA) probes (3Brain). A 100-μL droplet of medium containing 150K cells was placed on the recording area. After 1h incubation, 1.5 of ENS differentiation medium were added to the probe and replaced every 3-5 days. Recordings were performed at different time points. 1 minute of spontaneous activity was sampled from 4096 electrodes using the BioCAM system and analyzed using BrainWave 4 software. Spikes were detected using a sliding window algorithm on the raw channel traces applying a threshold for detection of 9 standard deviations. Bursts were defined as a minimum of 5 spikes occurring within a 100ms window in a given channel.

Synapse Quantification—Neural Crest cells were cultured for 28 days from the time of sacral or vagal specification. Cells were then fixed with 4% Paraformaldehyde for 15 minutes, permeabilized and blocked for 15 minutes at RT using blocking solution (0.1% Triton X-100 and 3 % BSA in PBS). Primary antibodies were diluted in blocking solution and cells were incubated at 4°C overnight under constant agitation. The following primary antibodies were used: Synapsin-1 (Rabbit, Cell Signaling Technologies #5297S, 1:1000), PSD-95 (Mouse, ThermoFisher #MA1-045, 1:500) and Map2 (Chicken, Abeam # ab5392, 1:2000). Cells were washed 2x with PBS with 0.5% Tween 20 (PBST) and then incubated with secondary antibodies and DAPI (1:1000) at RT for one hour under constant agitation. The following secondary antibodies were used: ThermoFisher Alexa Fluor Rabbit-488, Mouse-555, Chicken-647; all 1:500. Cells were then washed 3x with PBST and 1x with PBS. Images were acquired using a Nikon A1RHD25 confocal microscope equipped with a 20x oil objective using 2.5x optical zoom. Synapsin-1 and PSD95 puncta were manually counted using FIJI software[117], and Map2+ dendritic length was measured using the NeuronJ plugin[118].

The number of synapsin-1 and PSD95 puncta was normalized to 100μm dendritic length. A total of 3 independent differentiations were used for these experiments, and at least 3 images were taken per condition and differentiation.

QUANTIFICATION AND STATISTICAL ANALYSIS

Data are presented as Mean ± SD and were derived from at least three independent experiments. Data on replicates (n) is given in figure legends. Statistical analysis was performed using the Unpaired t-test, also known as Student's t-test (comparing two groups) or ANOVA with Dunnett test (comparing multiple groups against control). Distribution of the raw data approximated normal distribution.

Supplementary Material

Refer to Web version on PubMed Central for supplementary material.

DECLARATION OF INTERESTS

L.S. is a scientific co-founder and consultant and has received sponsored research support for work related to this study from Bluerock Therapeutics. L.S. and Y.F. are inventors of a patent application filed by Memorial Sloan Kettering Cancer Center on the methods described in this study. All other authors declare no competing interests.

REFERENCES

1. Gershon M (1999). The second brain: a groundbreaking new understanding of nervous disorders of the stomach and intestine (HarperCollins).
2. Bodian M, and Carter OO (1963). A family study of Hirschsprung's disease. Annals of Human Genetics 26, 261–277.
3. Whitehouse FR, and Kernohan JW (1948). Myenteric plexus in congenital megacolon: Study of Eleven Cases. Archives of Internal Medicine 82, 75–111. 10.1001/archinte.1948.00220250085005. [PubMed: 18110761]
4. Bolande RP (1974). The neurocristopathies: a unifying concept of disease arising in neural crest maldevelopment. Human pathology 5, 409–429.
5. Heanue TA, and Pachnis V (2007). Enteric nervous system development and Hirschsprung's disease: advances in genetic and stem cell studies. Nat Rev Neurosci 8, 466–479. 10.1038/nrn2137. [PubMed: 17514199]
6. N-Féketé C, Ricour C, Martelli H, Jacob SL, and Pellerin D (1986). Total colonic aganglionosis (with or without ileal involvement): a review of 27 cases. Journal of pediatric surgery 21, 251–254. [PubMed: 3958887]
7. Taraviras S, and Pachnis V (1999). Development of the mammalian enteric nervous system. Current opinion in genetics & development 9, 321–327. [PubMed: 10377293]
8. Hosoda K, Hammer RE, Richardson JA, Baynash AG, Cheung JC, Giaid A, and Yanagisawa M (1994). Targeted and natural (piebald-lethal) mutations of endothelin-B receptor gene produce megacolon associated with spotted coat color in mice. Cell 79, 1267–1276. [PubMed: 8001159]
9. Burns AJ, Goldstein AM, Newgreen DF, Stamp L, Schafer KH, Metzger M, Hotta R, Young HM, Andrews PW, Thapar N, et al. (2016). White paper on guidelines concerning enteric nervous system stem cell therapy for enteric neuropathies. Dev Biol 417, 229–251. 10.1016/j.ydbio.2016.04.001. [PubMed: 27059883]
10. Rao M, and Gershon MD (2016). The bowel and beyond: the enteric nervous system in neurological disorders. Nat Rev Gastroenterol Hepatol 13, 517–528. 10.1038/nrgastro.2016.107. [PubMed: 27435372]
11. Braak H, and Del Tredici K (2009). Neuroanatomy and Pathology of Sporadic Parkinson's Disease (Advances in anatomy, embryology and cell biology; 201) (Springer Berlin Heidelberg).
12. Braak H, Del Tredici K, Rüb U, De Vos RA, Steur ENJ, and Braak E (2003). Staging of brain pathology related to sporadic Parkinson's disease. Neurobiology of aging 24, 197–211. [PubMed: 12498954]

13. Rao M, and Gershon MD (2018). Enteric nervous system development: what could possibly go wrong? Nature Reviews Neuroscience 19, 552–565. [PubMed: 30046054]

14. Lake JI, and Heuckeroth RO (2013). Enteric nervous system development: migration, differentiation, and disease. Am J Physiol Gastrointest Liver Physiol 305, G1–24. 10.1152/ajpgi.00452.2012. [PubMed: 23639815]

15. Kapur RP (2000). Colonization of the murine hindgut by sacral crest-derived neural precursors: experimental support for an evolutionarily conserved model. Dev Biol 227, 146–155. 10.1006/dbio.2000.9886. [PubMed: 11076683]

16. Chambers SM, Qi Y, Mica Y, Lee G, Zhang X-J, Niu L, Bilsland J, Cao L, Stevens E, and Whiting P (2012). Combined small-molecule inhibition accelerates developmental timing and converts human pluripotent stem cells into nociceptors. Nature biotechnology 30, 715.

17. Menendez L, Yatskievych TA, Antin PB, and Dalton S (2011). Wnt signaling and a Smad pathway blockade direct the differentiation of human pluripotent stem cells to multipotent neural crest cells. Proceedings of the National Academy of Sciences 108, 19240–19245.

18. Hackland JOS, Frith TJR, Thompson O, Marin Navarro A, Garcia-Castro MI, Unger C, and Andrews PW (2017). Top-Down Inhibition of BMP Signaling Enables Robust Induction of hPSCs Into Neural Crest in Fully Defined, Xeno-free Conditions. Stem Cell Reports 9, 1043–1052.10.1016/j.stemcr.2017.08.008. [PubMed: 28919261]

19. Tchieu J, Zimmer B, Fattahi F, Amin S, Zeltner N, Chen S, and Studer L (2017). A Modular Platform for Differentiation of Human PSCs into All Major Ectodermal Lineages. Cell Stem Cell 21, 399–410 e397. 10.1016/j.stem.2017.08.015. [PubMed: 28886367]

20. Fattahi F, Steinbeck JA, Kriks S, Tchieu J, Zimmer B, Kishinevsky S, Zeltner N, Mica Y, El-Nachef W, Zhao H, et al. (2016). Deriving human ENS lineages for cell therapy and drug discovery in Hirschsprung disease. Nature 531, 105–109. 10.1038/naturel6951. [PubMed: 26863197]

21. Huang M, Miller ML, McHenry LK, Zheng T, Zhen Q, Ilkhanizadeh S, Conklin BR, Bronner ME, and Weiss WA (2016). Generating trunk neural crest from human pluripotent stem cells. Scientific Reports 6, 19121. 10.1038/srepl9727. [PubMed: 26750263]

22. Mica Y, Lee G, Chambers SM, Tomishima MJ, and Studer L (2013). Modeling neural crest induction, melanocyte specification, and disease-related pigmentation defects in hESCs and patient-specific iPSCs. Cell Rep 3, 1140–1152. 10.1016/j.celrep.2013.03.025. [PubMed: 23583175]

23. Frith TJ, Granata I, Wind M, Stout E, Thompson O, Neumann K, Stavish D, Heath PR, Ortmann D, Hackland JO, et al. (2018). Human axial progenitors generate trunk neural crest cells in vitro. Elife 7. 10.7554/eLife.35786.

24. Martyna Lukoseviciute SM, Tatjana Sauka-Spengler (2021). Neuromesodermal progenitor origin of trunk neural crest in vivo. Biorxiv. 10.1101/2021.02.10.430513.

25. Henrique D, Abranches E, Verrier L, and Storey KG (2015). Neuromesodermal progenitors and the making of the spinal cord. Development 142, 2864–2875. 10.1242/dev.119768. [PubMed: 26329597]

26. Gouti M, Tsakiridis A, Wymeersch FJ, Huang Y, Kleinjung J, Wilson V, and Briscoe J (2014). In vitro generation of neuromesodermal progenitors reveals distinct roles for wnt signalling in the specification of spinal cord and paraxial mesoderm identity. PLoS biology 12.

27. Lippmann ES, Williams CE, Ruhl DA, Estevez-Silva MC, Chapman ER, Coon JJ, and Ashton RS (2015). Deterministic HOX patterning in human pluripotent stem cell-derived neuroectoderm. Stem Cell Reports 4, 632–644. 10.1016/j.stemcr.2015.02.018. [PubMed: 25843047]

28. Tsakiridis A, and Wilson V (2015). Assessing the bipotency of in vitro-derived neuromesodermal progenitors. F1000Research 4. [PubMed: 26069726]

29. Hackland JOS, Shelar PB, Sandhu N, Prasad MS, Charney RM, Gomez GA, Frith TJR, and García-Castro MI (2019). FGF Modulates the Axial Identity of Trunk hPSC-Derived Neural Crest but Not the Cranial-Trunk Decision. Stem Cell Reports 12, 920–933. 10.1016/i.stemcr.2019.04.015. [PubMed: 31091435]

30. Tsakiridis A, Huang Y, Blin G, Skylaki S, Wymeersch F, Osorno R, Economou C, Karagianni E, Zhao S, Lowell S, and Wilson V (2014). Distinct Wnt-driven primitive streak-like populations

reflect in vivo lineage precursors. Development 141, 1209–1221. 10.1242/dev.101014. [PubMed: 24595287]

31. Turner DA, Hayward PC, Baillie-Johnson P, Rue P, Broome R, Faunes F, and Martinez Arias A (2014). Wnt/beta-catenin and FGF signalling direct the specification and maintenance of a neuromesodermal axial progenitor in ensembles of mouse embryonic stem cells. Development 141, 4243–4253. 10.1242/dev.112979. [PubMed: 25371361]
32. Rintala RJ, and Pakarinen MP (2012). Long-term outcomes of Hirschsprung's disease. Semin Pediatr Surg 21, 336–343. 10.1053/j.sempedsurg.2012.07.008. [PubMed: 22985839]
33. Neuvonen MI, Kyrklund K, Rintala RJ, and Pakarinen MP (2017). Bowel Function and Quality of Life After Transanal Endorectal Pull-through for Hirschsprung Disease: Controlled Outcomes up to Adulthood. Ann Surg 265, 622–629. 10.1097/sla.0000000000001695. [PubMed: 28169931]
34. Rothstein M, Bhattacharya D, and Simoes-Costa M (2018). The molecular basis of neural crest axial identity. Dev Biol 444 Suppl 1, S170–S180. 10.1016/j.ydbio.2018.07.026. [PubMed: 30071217]
35. Nakashima M, Toyono T, Akamine A, and Joyner A (1999). Expression of growth/differentiation factor 11, a new member of the BMP/TGFbeta superfamily during mouse embryogenesis. Mech Dev 80, 185–189. 10.1016/s0925-4773(98)00205-6. [PubMed: 10072786]
36. McPherron AC, Lawler AM, and Lee SJ (1999). Regulation of anterior/posterior patterning of the axial skeleton by growth/differentiation factor 11. Nat Genet 22, 260–264. 10.1038/10320. [PubMed: 10391213]
37. Liu JP (2006). The function of growth/differentiation factor 11 (Gdf11) in rostrocaudal patterning of the developing spinal cord. Development 133, 2865–2874. 10.1242/dev.02478. [PubMed: 16790475]
38. Suh J, Eom JH, Kim NK, Woo KM, Baek JH, Ryoo HM, Lee SJ, and Lee YS (2019). Growth differentiation factor 11 locally controls anterior-posterior patterning of the axial skeleton. J Cell Physiol 234, 23360–23368. 10.1002/jcp.28904. [PubMed: 31183862]
39. Jurberg AD, Aires R, Varela-Lasheras I, Nóvoa A, and Mallo M (2013). Switching axial progenitors from producing trunk to tail tissues in vertebrate embryos. Dev Cell 25, 451–462. 10.1016/j.devcel.2013.05.009. [PubMed: 23763947]
40. Szumska D, Pieles G, Essalmani R, Bilski M, Mesnard D, Kaur K, Franklyn A, El Omari K, Jefferis J, Bentham J, et al. (2008). VACTERL/caudal regression/Currarino syndrome-like malformations in mice with mutation in the proprotein convertase Pcsk5. Genes Dev 22, 1465–1477. 10.1101/gad.479408. [PubMed: 18519639]
41. Stauffer W, Sheng H, and Lim HN (2018). EzColocalization: An ImageJ plugin for visualizing and measuring colocalization in cells and organisms. Scientific Reports 8, 15764. 10.1038/s41598-018-33592-8. [PubMed: 30361629]
42. Zeltner N, Lafaille FG, Fattahi F, and Studer L (2014). Feeder-free derivation of neural crest progenitor cells from human pluripotent stem cells. JoVE (Journal of Visualized Experiments), e51609.
43. Burke AC, Nelson CE, Morgan BA, and Tabin C (1995). Hox genes and the evolution of vertebrate axial morphology. Development 121, 333–346. [PubMed: 7768176]
44. Akam M (1987). The molecular basis for metameric pattern in the Drosophila embryo. Development 101, 1–22.
45. Seller MJ, Embury S, Polani PE, and Adinolfi M (1979). Neural tube defects in curly-tail mice. II. Effect of maternal administration of vitamin A. Proceedings of the Royal Society of London. Series B. Biological Sciences 206, 95–107. [PubMed: 42072]
46. van den Berg DL, Snoek T, Mullin NP, Yates A, Bezstarosti K, Demmers J, Chambers I, and Poot RA (2010). An Oct4-centered protein interaction network in embryonic stem cells. Cell Stem Cell 6, 369–381. 10.1016/j.stem.2010.02.014. [PubMed: 20362541]
47. Chen W, Dong Q, Shin KH, Kim RH, Oh JE, Park NH, and Kang MK (2010). Grainyhead-like 2 enhances the human telomerase reverse transcriptase gene expression by inhibiting DNA methylation at the 5'-CpG island in normal human keratinocytes. J Biol Chem 285, 40852–40863. 10.1074/jbc.M110.103812. [PubMed: 20938050]

48. Hopkin AS, Gordon W, Klein RH, Espitia F, Daily K, Zeller M, Baldi P, and Andersen B (2012). GRHL3/GET1 and trithorax group members collaborate to activate the epidermal progenitor differentiation program. PLoS Genet 8, e1002829. 10.1371/journal.pgen.1002829. [PubMed: 22829784]

49. Lee YJ, McPherron A, Choe S, Sakai Y, Chandraratna RA, Lee SJ, and Oh SP (2010). Growth differentiation factor 11 signaling controls retinoic acid activity for axial vertebral development. Dev Biol 347, 195–203. 10.1016/j.ydbio.2010.08.022. [PubMed: 20801112]

50. Delva L, Bastie JN, Rochette-Egly C, Kraïba R, Balitrand N, Despouy G, Chambon P, and Chomienne C (1999). Physical and functional interactions between cellular retinoic acid binding protein II and the retinoic acid-dependent nuclear complex. Mol Cell Biol 19, 7158–7167. 10.1128/mcb.19.10.7158. [PubMed: 10490651]

51. Ghaffari H, and Petzold LR (2018). Identification of influential proteins in the classical retinoic acid signaling pathway. Theor Biol Med Model 15, 16–16. 10.1186/s12976-018-0088-7. [PubMed: 30322383]

52. Martínez-Morales PL, Diez del Corral R, Olivera-Martínez I, Quiroga AC, Das RM, Barbas JA, Storey KG, and Morales AV (2011). FGF and retinoic acid activity gradients control the timing of neural crest cell emigration in the trunk. Journal of Cell Biology 194, 489–503. 10.1083/jcb.201011077. [PubMed: 21807879]

53. Gont LK, Steinbeisser H, Blumberg B, and de Robertis EM (1993). Tail formation as a continuation of gastrulation: the multiple cell populations of the Xenopus tailbud derive from the late blastopore lip. Development 119, 991–1004. 10.1242/dev.119.4.991. [PubMed: 7916680]

54. Tzouanacou E, Wegener A, Wymeersch FJ, Wilson V, and Nicolas J-F (2009). Redefining the progression of lineage segregations during mammalian embryogenesis by clonal analysis. Developmental cell 17, 365–376. [PubMed: 19758561]

55. Amin S, Neijts R, Simmini S, van Rooijen C, Tan SC, Kester L, van Oudenaarden A, Creyghton MP, and Deschamps J (2016). Cdx and T Brachyury Co-activate Growth Signaling in the Embryonic Axial Progenitor Niche. Cell Rep 17, 3165–3177. 10.1016/j.celrep.2016.11.069. [PubMed: 28009287]

56. Cambray N, and Wilson V (2002). Axial progenitors with extensive potency are localised to the mouse chordoneural hinge. Development 129, 4855–4866. 10.1242/dev.129.20.4855. [PubMed: 12361976]

57. Le Douarin N, LeDouarin NM, and Kalcheim C (1999). The neural crest (Cambridge university press).

58. Hall BK, and Hörstadius S (1988). The neural crest: including a facsimile reprint of the neural crest by Sven Hörstadius (London; Toronto: Oxford University Press).

59. Burns AJ, Champeval D, and Le Douarin NM (2000). Sacral neural crest cells colonise aganglionic hindgut in vivo but fail to compensate for lack of enteric ganglia. Dev Biol 219, 30–43. 10.1006/dbio.1999.9592. [PubMed: 10677253]

60. Druckenbrod NR, and Epstein ML (2005). The pattern of neural crest advance in the cecum and colon. Dev Biol 287, 125–133. 10.1016/j.ydbio.2005.08.040. [PubMed: 16197939]

61. Bergner AJ, Stamp LA, Gonsalvez DG, Allison MB, Olson DP, Myers MG Jr., Anderson CR, and Young HM (2014). Birthdating of myenteric neuron subtypes in the small intestine of the mouse. J Comp Neurol 522, 514–527. 10.1002/cne.23423. [PubMed: 23861145]

62. Chalazonitis A, Pham TD, Li Z, Roman D, Guha U, Gomes W, Kan L, Kessler JA, and Gershon MD (2008). Bone morphogenetic protein regulation of enteric neuronal phenotypic diversity: relationship to timing of cell cycle exit. J Comp Neurol 509, 474–492. 10.1002/cne.21770. [PubMed: 18537141]

63. Pham TD, Gershon MD, and Rothman TP (1991). Time of origin of neurons in the murine enteric nervous system: sequence in relation to phenotype. Journal of comparative neurology 314, 789–798. [PubMed: 1816276]

64. Oh Y, Cho G-S, Li Z, Hong I, Zhu R, Kim M-J, Kim, Yong J, Tampakakis E, Tung L, Huganir R, et al. (2016). Functional Coupling with Cardiac Muscle Promotes Maturation of hPSC-Derived Sympathetic Neurons. Cell Stem Cell 19, 95–106. 10.1016/i.stem.2016.05.002. [PubMed: 27320040]

65. Baggiolini A, Callahan SJ, Montal E, Weiss JM, Trieu T, Tagore MM, Tischfield SE, Walsh RM, Suresh S, Fan Y, et al. (2021). Developmental chromatin programs determine oncogenic competence in melanoma. Science 373, eabc1048. 10.1126/science.abc1048. [PubMed: 34516843]
66. Weiss JM, Hunter MV, Cruz NM, Baggiolini A, Tagore M, Ma Y, Misale S, Marasco M, Simon-Vermot T, Campbell NR, et al. (2021). Anatomic position determines oncogenic specificity in melanoma. bioRxiv, 2020.2011.2014.383083. 10.1101/2020.11.14.383083.
67. Burns AJ, and Douarin NM (1998). The sacral neural crest contributes neurons and glia to the post-umbilical gut: spatiotemporal analysis of the development of the enteric nervous system. Development 125, 4335–4347. 10.1242/dev.125.21.4335. [PubMed: 9753687]
68. Le Douarin NM, and Teillet MA (1973). The migration of neural crest cells to the wall of the digestive tract in avian embryo. J Embryol Exp Morphol 30, 31–48. [PubMed: 4729950]
69. Huang T, Hou Y, Wang X, Wang L, Yi C, Wang C, Sun X, Tam PKH, Ngai SM, Sham MH, et al. (2022). Direct Interaction of Sox10 With Cadherin-19 Mediates Early Sacral Neural Crest Cell Migration: Implications for Enteric Nervous System Development Defects. Gastroenterology 162, 179–192.e111. 10.1053/j.gastro.2021.08.029. [PubMed: 34425092]
70. Foty RA, and Steinberg MS (2004). Cadherin-mediated cell-cell adhesion and tissue segregation in relation to malignancy. Int J Dev Biol 48, 397–409. 10.1387/ijdb.041810rf. [PubMed: 15349815]
71. Wilkinson DG (2021). Interplay of Eph-Ephrin Signalling and Cadherin Function in Cell Segregation and Boundary Formation. Frontiers in Cell and Developmental Biology 9. 10.3389/fcell.2021.784039.
72. Davy A, and Soriano P (2005). Ephrin signaling in vivo: look both ways. Dev Dyn 232, 1–10. 10.1002/dvdy.20200. [PubMed: 15580616]
73. Egea J, and Klein R (2007). Bidirectional Eph-ephrin signaling during axon guidance. Trends Cell Biol 17, 230–238. 10.1016/j.tcb.2007.03.004. [PubMed: 17420126]
74. Kullander K, and Klein R (2002). Mechanisms and functions of Eph and ephrin signalling. Nat Rev Mol Cell Biol 3, 475–486. 10.1038/nrm856. [PubMed: 12094214]
75. Rohani N, Canty L, Luu O, Fagotto F, and Winklbauer R (2011). EphrinB/EphB signaling controls embryonic germ layer separation by contact-induced cell detachment. PLoS Biol 9, e1000597. 10.1371/journal.pbio.1000597. [PubMed: 21390298]
76. Beck M, Schlabrakowski A, Schrödl F, Neuhuber W, and Brehmer A (2009). ChAT and NOS in human myenteric neurons: co-existence and co-absence. Cell Tissue Res 338, 37–51. 10.1007/s00441-009-0852-4. [PubMed: 19711100]
77. Le Douarin NM, and Teillet M-AM (1974). Experimental analysis of the migration and differentiation of neuroblasts of the autonomic nervous system and of neurectodermal mesenchymal derivatives, using a biological cell marking technique. Developmental Biology 41, 162–184. 10.1016/0012-1606(74)90291-7. [PubMed: 4140118]
78. Le Lièvre CS, and Le Douarin NM (1975). Mesenchymal derivatives of the neural crest: analysis of chimaeric quail and chick embryos. J Embryol Exp Morphol 34, 125–154. [PubMed: 1185098]
79. Le Douarin NM, Creuzet S, Couly G.r., and Dupin E (2004). Neural crest cell plasticity and its limits. Development 131, 4637–4650. 10.1242/dev.01350. [PubMed: 15358668]
80. Le Douarin N, and Kalcheim C (1999). The Neural Crest, 2 Edition (Cambridge University Press). DOI: 10.1017/CBO9780511897948.
81. Tang W, and Bronner ME (2020). Neural crest lineage analysis: from past to future trajectory. Development 147. 10.1242/dev.193193.
82. Rocha M, Beiriger A, Kushkowski EE, Miyashita T, Singh N, Venkataraman V, and Prince VE (2020). From head to tail: regionalization of the neural crest. Development 147. 10.1242/dev.193888.
83. Abzhanov A, Tzahor E, Lassar AB, and Tabin CJ (2003). Dissimilar regulation of cell differentiation in mesencephalic (cranial) and sacral (trunk) neural crest cells in vitro.
84. Couly G, Creuzet S, Bennaceur S, Vincent C, and Le Douarin NM (2002). Interactions between Hox-negative cephalic neural crest cells and the foregut endoderm in patterning the facial skeleton in the vertebrate head.
85. Lwigale PY, Conrad GW, and Bronner-Fraser M (2004). Graded potential of neural crest to form cornea, sensory neurons and cartilage along the rostrocaudal axis.

86. Srinivasan A, and Toh YC (2019). Human Pluripotent Stem Cell-Derived Neural Crest Cells for Tissue Regeneration and Disease Modeling. Front Mol Neurosci 12, 39. 10.3389/fnmol.2019.00039. [PubMed: 30853889]

87. Wiese CB, Deal KK, Ireland SJ, Cantrell VA, and Southard-Smith EM (2017). Migration pathways of sacral neural crest during development of lower urogenital tract innervation. Developmental Biology 429, 356–369. 10.1016/i.vdbio.2017.04.011. [PubMed: 28449850]

88. ten Berge D, Brugmann SA, Helms JA, and Nusse R (2008). Wnt and FGF signals interact to coordinate growth with cell fate specification during limb development. Development 135, 3247–3257. 10.1242/dev.023176. [PubMed: 18776145]

89. Aires R, de Lemos L, Nóvoa A, Jurberg AD, Mascrez B, Duboule D, and Mallo M (2019). Tail Bud Progenitor Activity Relies on a Network Comprising Gdf11, Lin28, and Hox13 Genes. Developmental Cell 48, 383–395.e388. [PubMed: 30661984]

90. Sato T, Kataoka K, Ito Y, Yokoyama S, Inui M, Mori M, Takahashi S, Akita K, Takada S, and Ueno-Kudoh H (2020). Lin28a/let-7 pathway modulates the Hox code via Polycomb regulation during axial patterning in vertebrates. Elite 9, e53608.

91. Denham M, Hasegawa K, Menheniott T, Rollo B, Zhang D, Hough S, Alshawaf A, Febbraro F, Ighaniyan S, and Leung J (2015). Multipotent caudal neural progenitors derived from human pluripotent stem cells that give rise to lineages of the central and peripheral nervous system. Stem cells 33, 1759–1770. [PubMed: 25753817]

92. von Kolliker A (1884). Die embryonalen Keimblätter und die Gewebe (Wilhelm Engelmann).

93. Brown JM, and Storey KG (2000). A region of the vertebrate neural plate in which neighbouring cells can adopt neural or epidermal fates. Current Biology 10, 869–872. [PubMed: 10899008]

94. limura T, and Pourquié O (2006). Collinear activation of Hoxb genes during gastrulation is linked to mesoderm cell ingression. Nature 442, 568–571. [PubMed: 16760928]

95. Cambray N, and Wilson V (2007). Two distinct sources for a population of maturing axial progenitors.

96. Olivera-Martinez I, Harada H, Halley PA, and Storey KG (2012). Loss of FGF-dependent mesoderm identity and rise of endogenous retinoid signalling determine cessation of body axis elongation. PLoS biology 10, e1001415. [PubMed: 23118616]

97. Zhang D, Rollo BN, Nagy N, Stamp L, and Newgreen DF (2019). The enteric neural crest progressively loses capacity to form enteric nervous system. Dev Biol 446, 34–42. 10.1016/j.ydbio.2018.11.017. [PubMed: 30529057]

98. Cederquist GY, Asciolla JJ, Tchieu J, Walsh RM, Cornacchia D, Resh MD, and Studer L (2019). Specification of positional identity in forebrain organoids. Nature biotechnology 37, 436–444.

99. Cornacchia D, Zhang C, Zimmer B, Chung SY, Fan Y, Soliman MA, Tchieu J, Chambers SM, Shah H, and Pauli D (2019). Lipid deprivation induces a stable, naïve-to-primed intermediate state of pluripotency in human PSCs. Cell stem cell 25, 120–136. ellO. [PubMed: 31155483]

100. Frykman PK, Cheng Z, Wang X, and Dhall D (2015). Enterocolitis causes profound lymphoid depletion in endothelin receptor B-and endothelin 3-null mouse models of Hirschsprung-associated enterocolitis. European journal of immunology 45, 807–817. [PubMed: 25487064]

101. Dobin A, Davis CA, Schlesinger F, Drenkow J, Zaleski C, Jha S, Batut P, Chaisson M, and Gingeras TR (2013). STAR: ultrafast universal RNA-seq aligner. Bioinformatics 29,15–21. [PubMed: 23104886]

102. Engström PG, Steijger T, Sipos B, Grant GR, Kahles A, Rätsch G, Goldman N, Hubbard TJ, Harrow J, and Guigó R (2013). Systematic evaluation of spliced alignment programs for RNA-seq data. Nature methods 10, 1185–1191. [PubMed: 24185836]

103. Love MI, Huber W, and Anders S (2014). Moderated estimation of fold change and dispersion for RNA-seq data with DESeq2. Genome Biology 15, 550. 10.1186/sl3059-014-0550-8. [PubMed: 25516281]

104. Buenrostro JD, Giresi PG, Zaba LC, Chang HY, and Greenleaf WJ (2013). Transposition of native chromatin for fast and sensitive epigenomic profiling of open chromatin, DNA-binding proteins and nucleosome position. Nat Methods 10, 1213–1218. 10.1038/nmeth.2688. [PubMed: 24097267]

105. Li H, and Durbin R (2009). Fast and accurate short read alignment with Burrows–Wheeler transform. Bioinformatics 25, 1754–1760. 10.1093/bioinformatics/btp324. [PubMed: 19451168]
106. Li H, Handsaker B, Wysoker A, Fennell T, Ruan J, Homer N, Marth G, Abecasis G, Durbin R, and Genome Project Data Processing, S. (2009). The Sequence Alignment/Map format and SAM tools. Bioinformatics (Oxford, England) 25, 2078–2079. 10.1093/bioinformatics/btp352. [PubMed: 19505943]
107. Institute, B. “Picard Tools.” Broad Institute, GitHub repository. .
108. Liu T (2014). Use model-based Analysis of ChIP-Seq (MACS) to analyze short reads generated by sequencing protein-DNA interactions in embryonic stem cells. Methods Mol Biol 1150, 81–95. 10.1007/978-l-4939-0512-6_4. [PubMed: 24743991]
109. Brown R.S.a.G. (2022). DiffBind: Differential binding analysis of ChIPSeq peak data.
110. Ramírez F, Ryan DP, Grüning B, Bhardwaj V, Kilpert F, Richter AS, Heyne S, Dündar F, and Manke T (2016). deepTools2: a next generation web server for deep-sequencing data analysis. Nucleic Acids Res 44, W160–165. 10.1093/nar/gkw257. [PubMed: 27079975]
111. Amemiya HM, Kundaje A, and Boyle AP (2019). The ENCODE Blacklist: Identification of Problematic Regions of the Genome. Scientific reports 9, 9354–9354. 10.1038/s41598-019-45839-z. [PubMed: 31249361]
112. Zhong A, Li M, and Zhou T (2020). Protocol for the Generation of Human Pluripotent Reporter Cell Lines Using CRISPR/Cas9. STAR Protoc 1. 10.1016/j.xpro.2020.100052.
113. Israelyan N, Del Colle A, Li Z, Park Y, Xing A, Jacobsen JPR, Luna RA, Jensen DD, Madra M, Saurman V, et al. (2019). Effects of Serotonin and Slow-Release 5-Hydroxytryptophan on Gastrointestinal Motility in a Mouse Model of Depression. Gastroenterology 157, 507–521.e504. 10.1053/j.gastro.2019.04.022. [PubMed: 31071306]
114. Margolis KG, Li Z, Stevanovic K, Saurman V, Israelyan N, Anderson GM, Snyder I, Veenstra-VanderWeele J, Blakely RD, and Gershon MD (2016). Serotonin transporter variant drives preventable gastrointestinal abnormalities in development and function. J Clin Invest 126, 2221–2235. 10.1172/jci84877. [PubMed: 27111230]
115. Swaminathan M, Hill-Yardin E, Ellis M, Zygorodimos M, Johnston LA, Gwynne RM, and Bornstein JC (2016). Video Imaging and Spatiotemporal Maps to Analyze Gastrointestinal Motility in Mice. J Vis Exp, 53828. 10.3791/53828. [PubMed: 26862815]
116. Hung LY, Parathan P, Boonma P, Wu Q, Wang Y, Haag A, Luna RA, Bornstein JC, Savidge TC, and Foong JPP (2020). Antibiotic exposure postweaning disrupts the neurochemistry and function of enteric neurons mediating colonic motor activity. Am J Physiol Gastrointest Liver Physiol 318, G1042–g1053. 10.1152/ajpgi.00088.2020. [PubMed: 32390463]
117. Schindelin J, Arganda-Carreras I, Frise E, Kaynig V, Longair M, Pietzsch T, Preibisch S, Rueden C, Saalfeld S, Schmid B, et al. (2012). Fiji: an open-source platform for biological-image analysis. Nat Methods 9, 676–682. 10.1038/nmeth.2019.. [PubMed: 22743772]
118. Meijering E, Jacob M, Sarria JC, Steiner P, Hirling H, and Unser M (2004). Design and validation of a tool for neurite tracing and analysis in fluorescence microscopy images. Cytometry A 58, 167–176. 10.1002/cyto.a.20022 [PubMed: 15057970]

Highlights

1. GDF11 enables transition from trunk to sacral neural crest in human PSCs.
2. Posterior neural crest emerges via a neuro-mesodermal progenitor in vitro.
3. Vagal and sacral neural crest exhibit distinct migratory behaviors.
4. Combined vagal/sacral neural crest injection induces rescue in severe HSCR model.

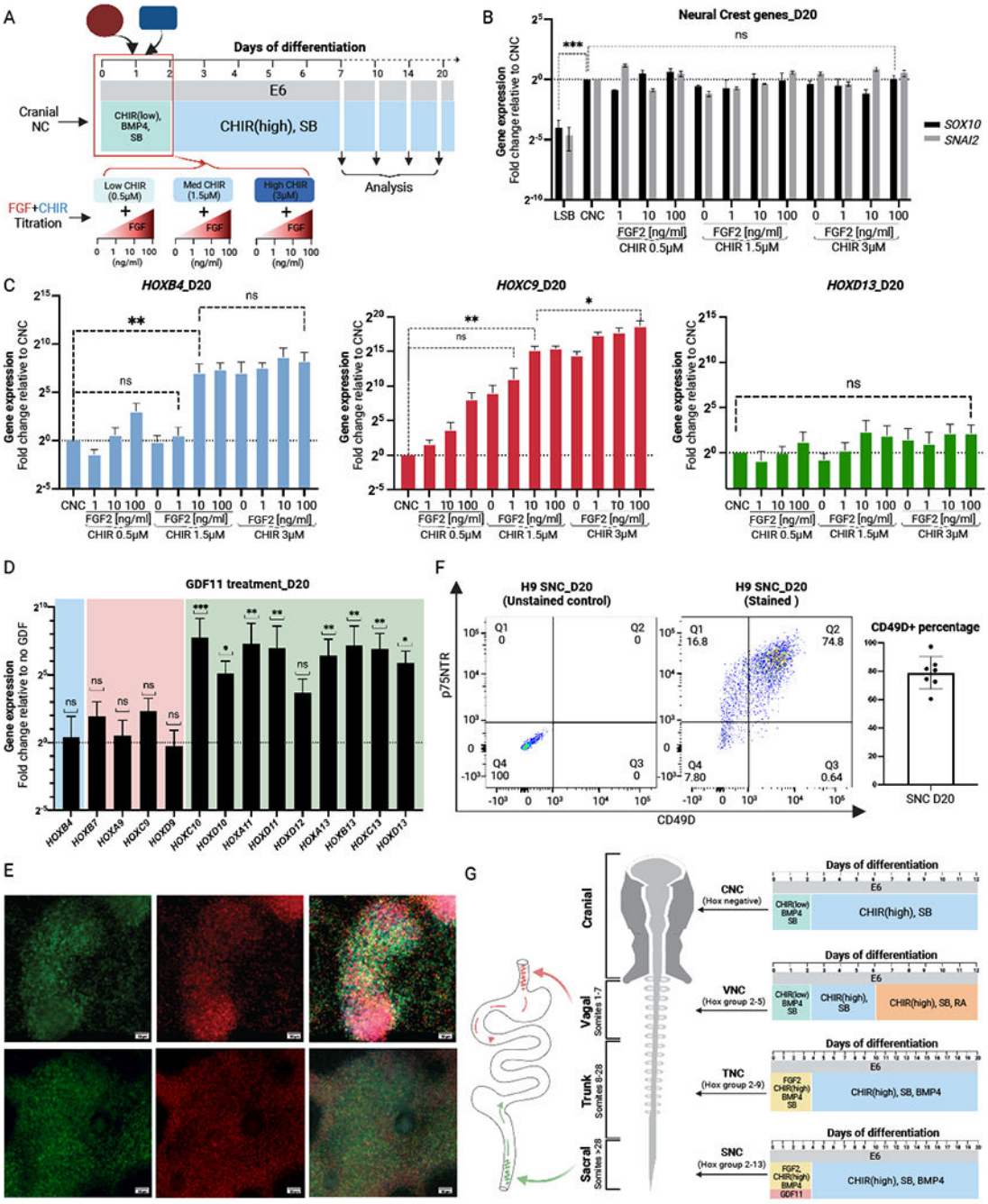

Figure 1. |. Derivation of sacral NC from hPSCs

(A) Diagram of the FGF and CHIR titration experiment.

(B) qRT-PCR of neural crest genes at D20 under all conditions compared with LSB control, which generates neurectoderm. CNC, cranial neural crest. N= 3 biological replicates.

(C) qRT-PCR of *HOX* genes that indicate regional identity corresponding to distinct axial levels at D20. *HOXB4*: vagal level; *HOXC9:* trunk level; *HOXD13:* sacral level. N= 4 biological replicates

(D) qRT-PCR of *HOX* genes with or without GDF11 at D20. N= 3 biological replicates.

(E) Immunocytochemistry of sacral NC at D20. Co-staining for SOX10 with posterior HOX proteins HOXC9 and HOXD13 shows most cells become sacral NC. Scale bars, 50 μm.
(F) Flow cytometry of sacral NC for CD49D and p75NTR at D20. Left: representative plot. Right: quantitative data of CD49D+ cell percentage. N= 7 biological replicates.
(G) Summary of protocols that generate NC cells at different axial levels.
Data are present as Mean ± SEM; Statistical analysis was performed using the Unpaired t-test or ANOVA with Dunnett test.

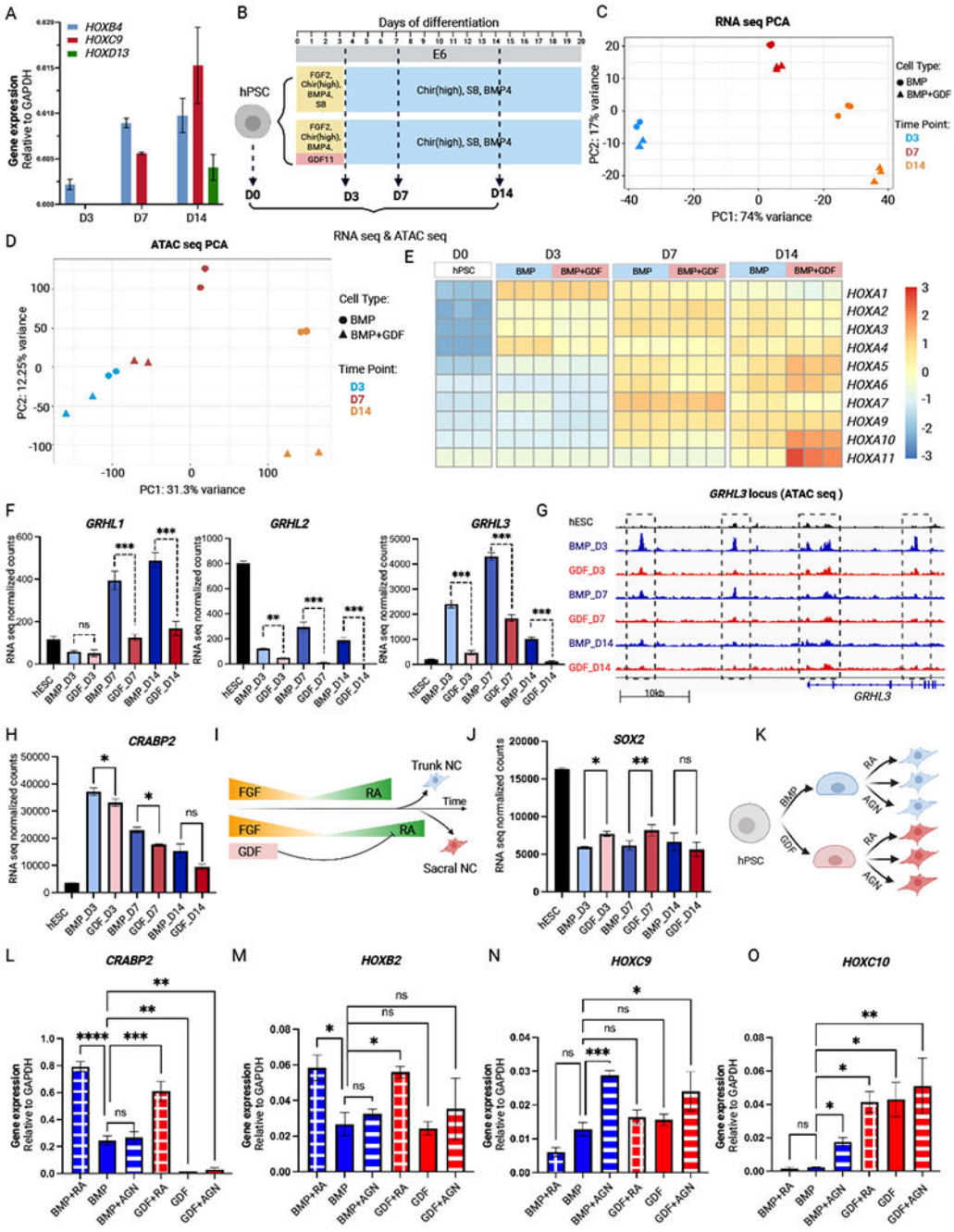

Figure 2. |. GDF11-mediated expression of 5' *HOX* genes via modulation of RA signaling

(A) qRT-PCR analysis showing the progressive expression of *HOX* genes from 3' to 5'. N= 4 biological replicates.

(B) Diagram of RNA seq and ATAC seq experiments.

(C-D) PCA plots of the RNA and ATAC sequencing data respectively.

(E) Heat map of HOXA genes, showing increased expression of *HOXA* genes over time and greater expression of posterior *HOXA* genes under GDF11 treatment. Presented as normalized counts scaled by row.

(F) Expression of GRHL factors from RNA seq. N= 3 biological replicates.
(G) Chromatin accessibility status of *GRHL3* locus from ATAC seq. N= 3 biological replicates.
(H) Expression of RA binding protein *CRABP2*. N= 3 biological replicates.
(I) Schematic drawing of proposed mechanism where GDF11 promotes the generation of sacral NC by RA inhibition.
(J) Expression of stem cell marker *SOX2*. N= 3 biological replicates.
(K) Experimental design to test the RA hypothesis.
(L-O) qRT-PCR data showing expression of various genes related to RA signaling and AP identity for the experiment depicted in (K), N= 3 biological replicates. (L) Expression of *CRABP2,* confirming the effect of RA and RA inhibitor AGN. (M-O) *HOXB2* was promoted by RA and *HOXC9* and *HOXC10* was promoted by RA inhibition.
RNA sequencing data presented as counts normalized using the Median of Ratios method (DESeq2). Data are presented as mean ± SEM; Statistical analysis was performed using the unpaired t-test or ANOVA with Dunnett test.

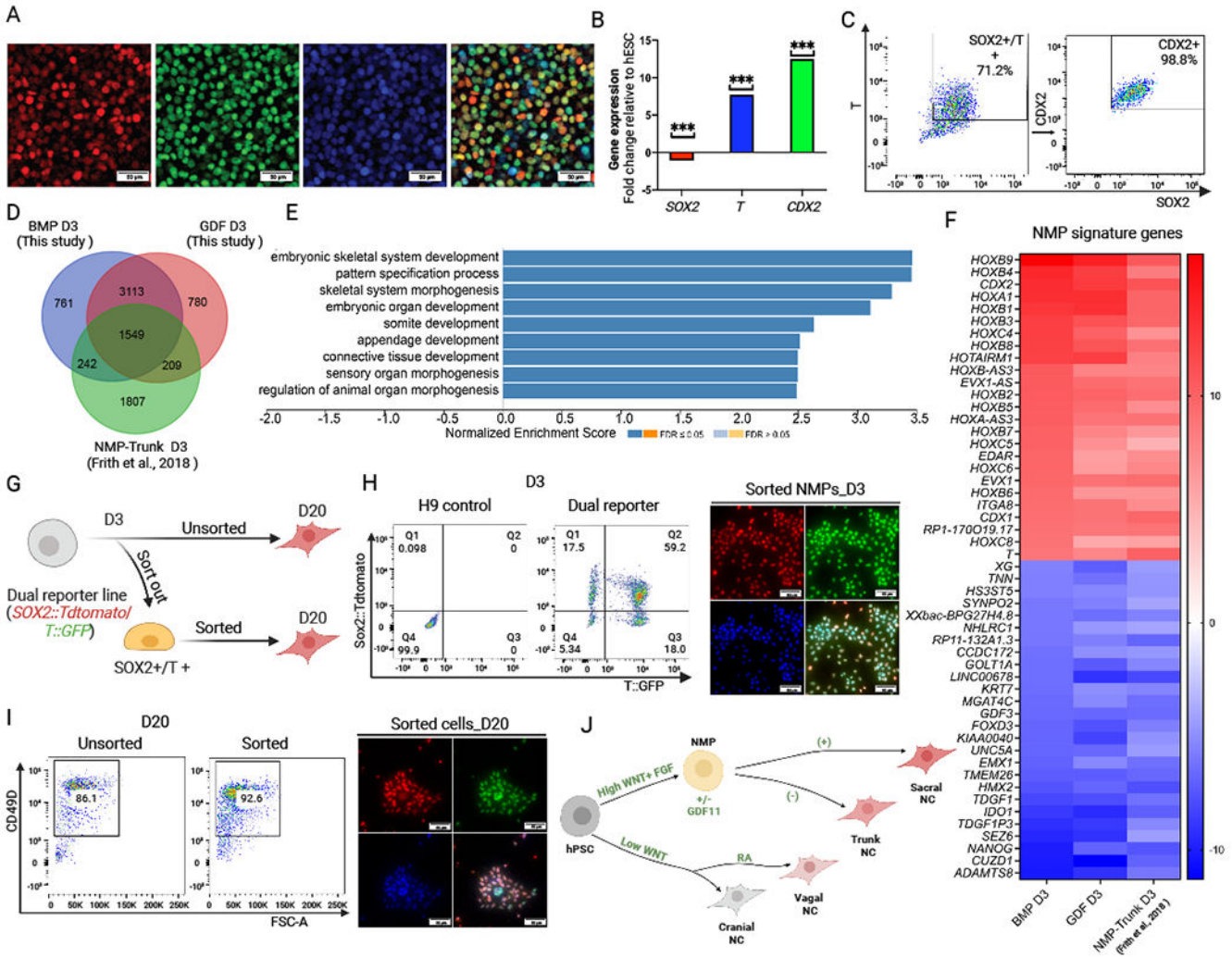

Figure 3. |. Sacral NC cells are derived from an NMP-like posterior precursors

(A-C) Analysis of D3 cells for expression of NMP key markers: *SOX2, T* and *CDX2*, by IF (A), qRT-PCR (B) and flow cytometry (C), showing most cells are triple-positive NMPs. N= 3 biological replicates. Scale bars, 50 μm.

(D) Venn diagram of differentially expressed genes (|log2(FC)|>1) representing D3 cells of our trunk differentiation protocol (BMP D3), sacral differentiation (GDF D3) and D3 NMP cells from Frith et al., study (NMP-Trunk D3) [23].

(E) GO analysis of GDF D3 cells.

(F) Top 25 most up and down regulated genes from the common genes in the Venn diagram.

(G) Experimental design depicting use of *SOX2*::TdTomato and *T*::GFP dual reporter hESC line to test if a pure NMP-like population can give rise to sacral NC.

(H) Flow cytometry data of D3 cells using dual reporter line or H9 WT control (left). Purity of sorted NMPs is confirmed with immunostaining for SOX2 and T (right). Scale bars, 50 μm.

(I) Flow cytometry data of D20 cells from unsorted and sorted NMPs (left). The sacral NC identity from pure NMPs is confirmed with immunostaining of SOX10 and HOXD13 (right). Scale bars, 50 μm.

(J) Summary of anterior and posterior NC domains originating from different precursors. Data are presented as mean ± SEM; Statistical analysis was performed using the unpaired t-test.

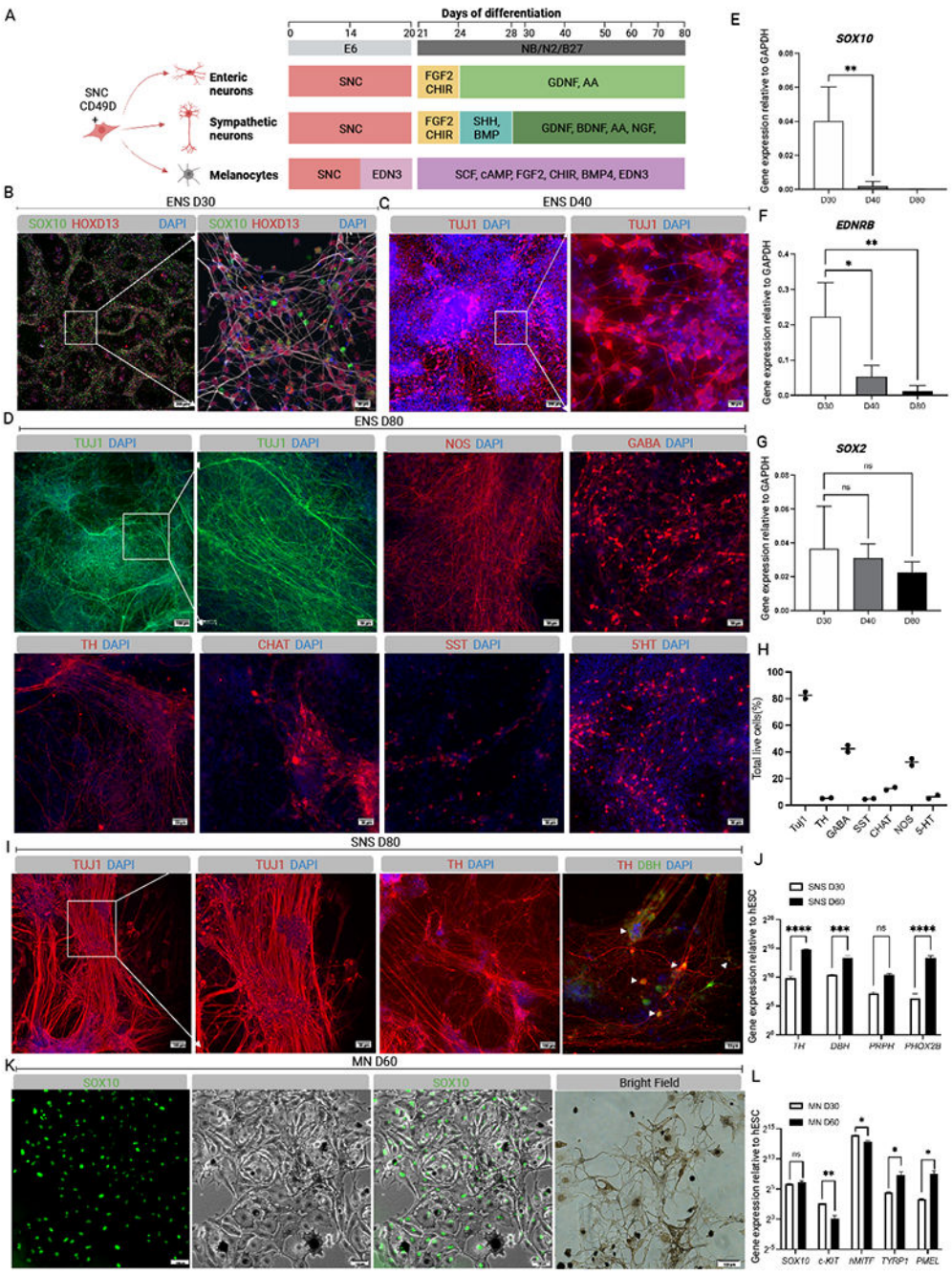

Figure 4. |. Sacral NC can be directed to diverse enteric and non-enteric fates

(A) Diagram of protocols to specify sacral NC cells towards enteric neurons (ENS, upper), sympathetic neurons (SNS, middle) and melanocytes (MN, bottom).

(B-D) Immunostaining of cells at D30 (B), D40 (C) and D80 (D), indicating cells transit from sacral precursors (B) to mature neurons that contains different subtypes (D). Scale bars, 50 μm.

(E-G) Gene expression of NC marker *SOX10*, enteric NC precursor marker *EDNRB* and neuronal marker *SOX2* over time. N= 3 biological replicates.

(H) Neuron subtype composition within the culture at D80. N= 2 biological replicates.
(I) Immunostaining of SNS at D80. Neurons form bundle-like structures composed of long neurites. Scale bars, 100 μm (left) and 50 μm (the rest).
(J) Gene expression of sympathetic neuronal markers over time. N= 4 biological replicates.
(K) Live imaging of MN at D60 using a *SOX10*::GFP reporter line under florescent microscope (left 3 panels) and BF microscope (right panel), showing continuous expression of *SOX10* and pigmentation. Scale bars, 100 μm.
(L) Expression of melanocyte markers: *SOX10, hMITF, c-KIT* and pigment-related genes *TYPL1 PMEL* over time. N= 3 biological replicates.
Data are presented as mean ± SEM; Statistical analysis was performed using the ANOVA with Dunnett test.

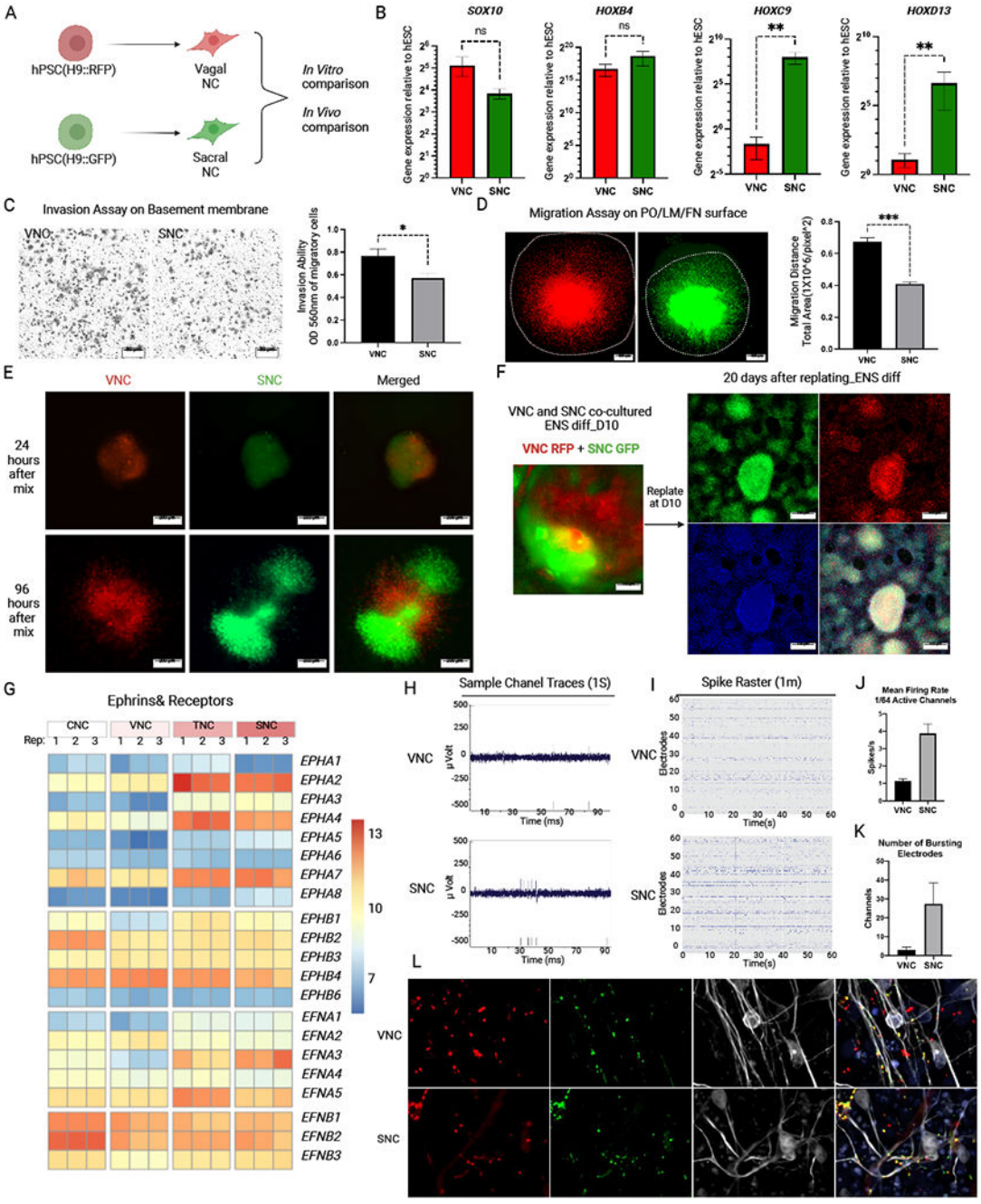

Figure 5. |. Vagal and Sacral NC exhibits distinct behavior *in vitro*

(A) Schematic drawing of experimental design. RFP-tagged hPSC line was used for vagal lineages and GFP-tagged line for sacral lineages.

(B) qRT-PCR of *SOX10* and *HOX* genes to confirm the VNC and SNC identity. N= 6 biological replicates.

(C) Invasion assay of VNC and SNC. Cells crossed the membrane are visualized (left) and quantified using plater reader (right). Scale bars, 50 μm. N= 3 biological replicates.

(D) Migration assay of VNC and SNC on PO/LM/FN surface. Cells migrated out of spherical aggregate were imaged (left) and migration distance were quantified (right). Scale bars, 500 μm. N= 3 biological replicates.
(E) 3D Matrigel embedded migration assay of co-cultured VNC and SNC. Fluorescence image of cells at 24 hours (upper) and 96 hours (lower), show self-sorting activity. Scale bars, 500 μm.
(F) Co-cultured VNC (red) and SNC (green) cells undergoing ENS differentiation with replating at D10. Scale bars, 100 μm.
(G) Heat map of cadherins in NC samples of different axial levels. Presented as normalized counts.
(H) Representative traces of electrical activity in NC-derived neurons as recorded by MEA system in over a period of 1 second. (I) Spike raster gram showing 1 m of activity. (J-K) Quantification of mean firing rate and number of bursting electrodes.
(L) Immunostaining of synaptic markers in enteric neurons derived from VNC and SNC. Data are presented as mean ± SEM; Statistical analysis was performed using the unpaired t-test.

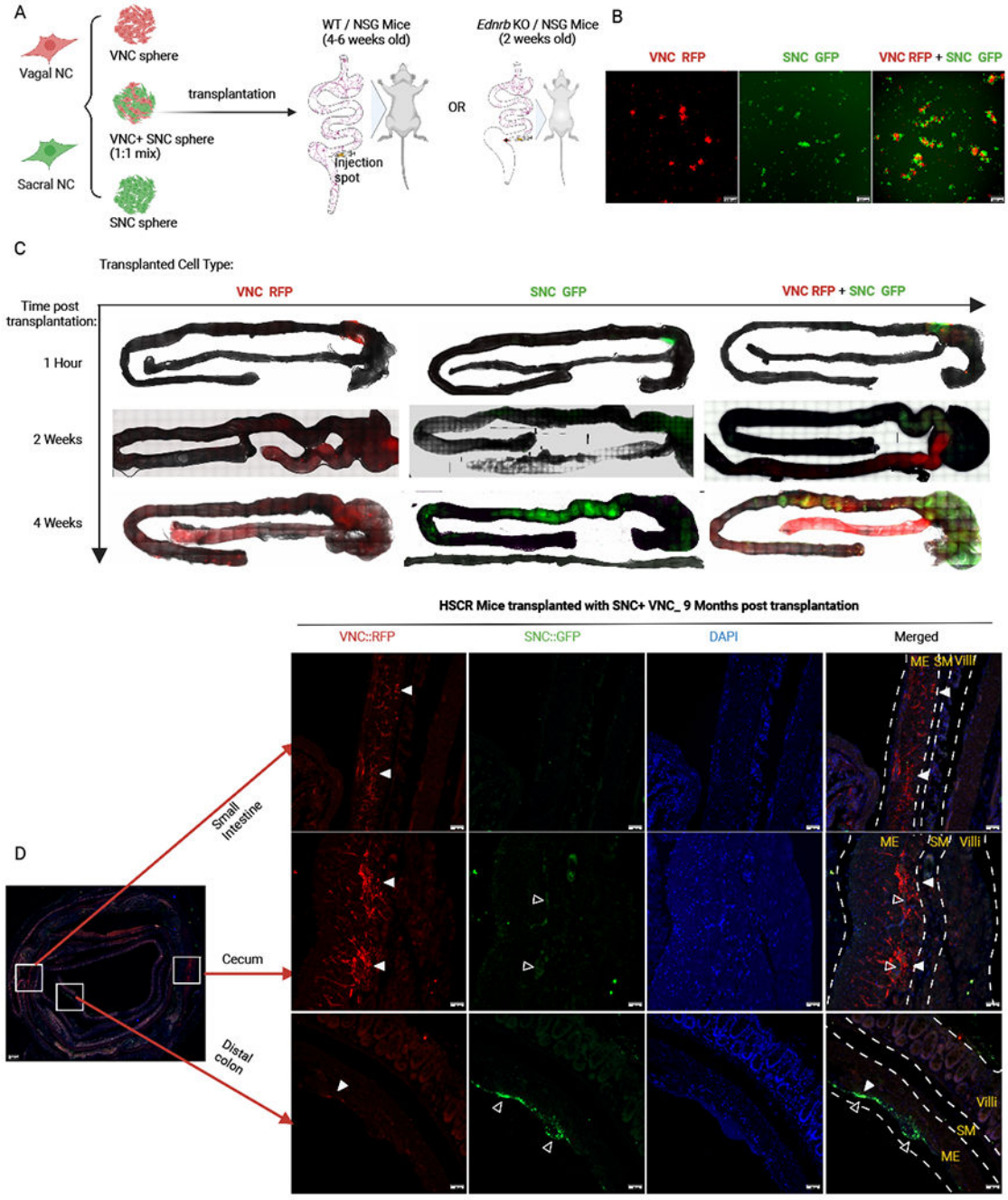

Figure 6. Vagal and Sacral NC exhibits distinct behavior *in vivo*

(A-B) Schematic drawing of mice transplantation experiments. NC cells are cultured under non-adherent conditions to form small spheres composed of either vagal, sacral, or combined vagal/sacral NC and injected into the mouse cecum.

(C) Fluorescent images of mouse gut that were transplanted with different axial types of NC cells: VNC (left), SNC (middle), VNC+SNC (right). The images are taken at sequential time points after transplantation: 1 Hour (upper), 2 weeks (middle), 4 weeks (bottom).

(D) Immunostaining of 9-month-old KO mouse that received VNC+SNC transplantation. RFP for VNC, indicated by white solid arrows and GFP for SNC, indicated by open arrows. Small intestine (upper); Cecum (middle), Distal colon (bottom). Scale bars, 100 μm.

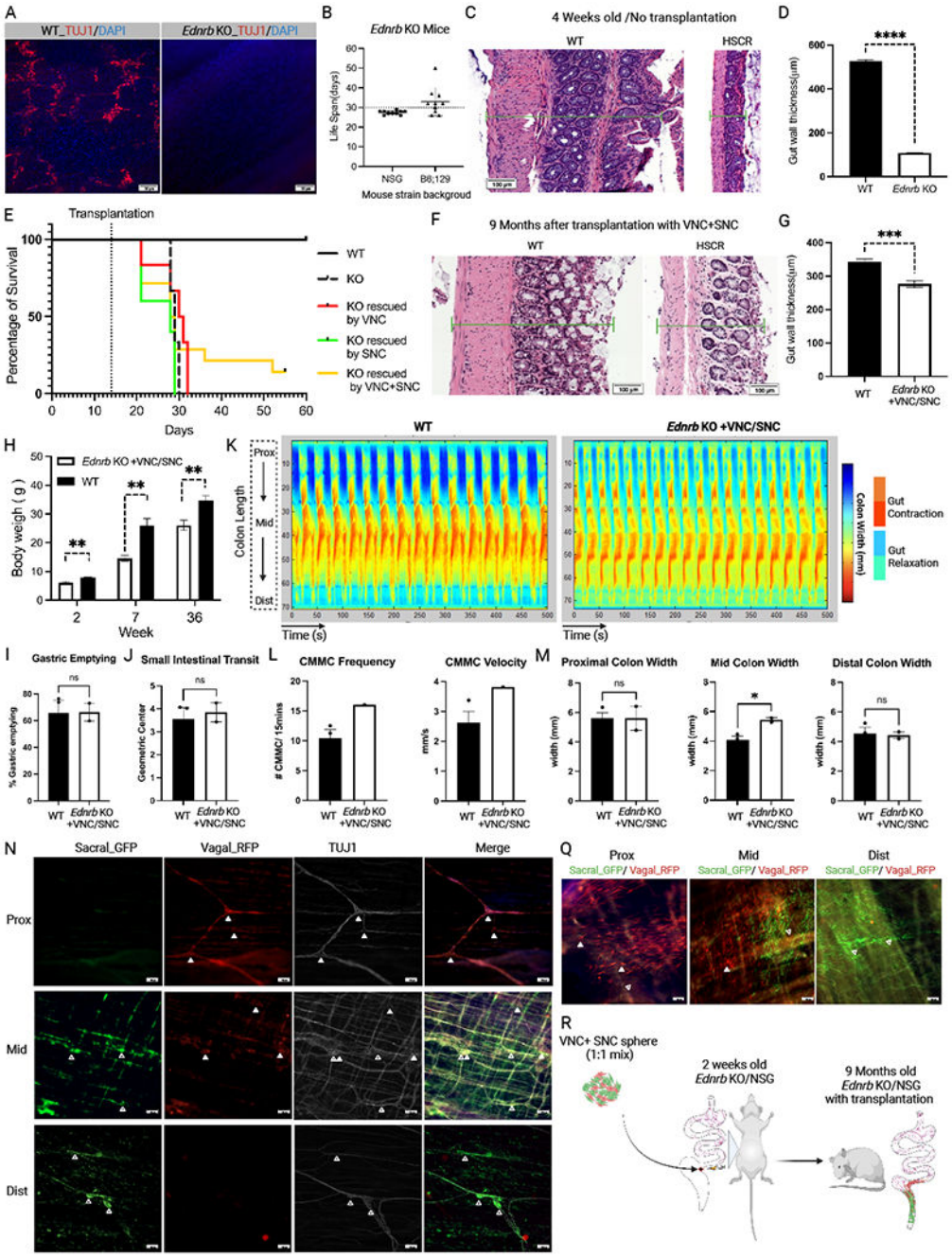

Figure 7. Developing a cell-based therapy for HSCR disease in *Ednrb* KO mouse model

(A) Staining with TUJ1 in distal colon of WT and *Ednrb* KO (HSCR) mice. Scale bars, 50 μm.

(B) Comparison of life spans of *Ednrb* KO mice in different genetic backgrounds. N= 10 different mice.

(C-D) Gut wall thickness in distal colon of 4-week-old WT and HSCR mice without any treatment. Scale bars, 100 μm.

(E) Survival curve of NSG/*Ednrb* KO mice that received various transplantation paradigms. N=12 for KO grafted with VNC+SNC and N= 7 mice for all other groups.
(F-G) Gut wall thickness of 9-month-old WT and HSCR mice with VNC+SNC transplantation. Scale bars, 100 μm.
(H) Body weight of WT mice and HSCR mice with VNC+SNC transplantation post transplantation. N= 3 different mice.
(I-J) Gastric emptying and SI transit measured by rhodamine dextran dye gavage. N= 3 different mice for WT. N= 2 different mice for *Ednrb* KO.
(K-M) Representative spatiotemporal maps and quantification of video imaging of colonic migration motor complexes (CMMCs) in 9 months old WT mice and rescued HSCR mice. Completed CMMCs in rescued mice indicated restored ENS function. N= 3 different mice for WT. N= 2 different mice for *Ednrb* KO.
(N-Q) Wholemount staining for neurons (N) and non-neurons (Q) of 9-month-old rescued HSCR mouse. RFP for VNC (solid arrows) and GFP for SNC (open arrows). Scale bars, 100 μm.
(R) Schematic drawing to illustrate combined VNC and SNC transplantation rescues severe HSCR.
Data are presented as mean ± SEM; Statistical analysis was performed using the unpaired t-test.

KEY RESOURCE TABLE

REAGENT or RESOURCE	SOURCE	IDENTIFIER
Antibodies		
Goat anti SOX10	Santa Cruz	Cat#sc-17342, RRID:AB_2195374
Mouse anti SOX10	Santa Cruz	Cat#sc-365692, RRID:AB_10844002
Mouse anti HOXC9	Abcam	Cat#ab50839, RRID:AB_880494
Rabbit anti HOXD13	Abcam	Cat#ab19866, RRID:AB_733004
Mouse anti Ki67	Dako	Cat# M7240, RRID:AB_2142367
Mouse anti CDX2	BioGenex	Cat#MU392A-5UC, RRID:AB_2650531
Goat anti Bra/T	R&D Systems	Cat#AF2085 , RRID:AB_2200235
Rabbit anti SOX2	Cell signaling Tech	Cat#35795, RRID:AB_2195767
PE conjugated Mouse Anti-Human CDX-2	BD Biosciences	Cat#563428, RRID:AB_2738198)
APC-conjugated Human/Mouse Bra/T	R&D Systems	Cat#IC2085A, RRID:AB_2891298
Alexa Fluor® 488 Mouse anti-Sox2 Clone O30-678	BD Biosciences	Cat#561593, RRID:AB_10894382
Rabbit anti SNAI2	Cell signaling Tech	Cat#9585, RRID:AB_2239535
Rabbit anti TUJ1	Covance	Cat#MMS-435P, RRID:AB_2313773
Chicken anti TUJ1	Abcam	Cat#ab107216, RRID:AB_10899689
Mouse anti TUJ1	Biolegend	Cat#801201, RRID:AB_2313773
Rabbit anti GABA	Sigma	Cat#A2052, RRID:AB_477652
Mouse anti TH	Immunostar	Cat#22941, RRID:AB_572268
Rabbit anti nNOS	Millipore	Cat#07-571, RRID:AB_11211970
Goat anti CHAT	Millipore	Cat#AB144P, RRID:AB_2079751
Rabbit anti 5'HT	Sigma	Cat#S5545, RRID:AB_477522
Rabbit anti SST	Millipore	Cat#mab354, RRID:AB_2255365
Rabbit anti DBH	ImmunoStar	Cat#22806, RRID:AB_572229
Rabbit ISL1	Developmental Studies Hybridoma Bank	Cat#39.4D5, RRID:AB_2314683
Rabbit anti S100-beta	Abcam	Cat# ab52642, RRID:AB_882426
PE/Cy7 conjugated CD49D	Biolegend	Cat#304314, RRID:AB_10643278
APC conjugated CD49D	Biolegend	Cat#304308, RRID:AB_2130041
PE conjugated HNK1	Biolegend	Cat#359611, RRID:AB_2562758
APC conjugated P75NTR	Biolegend	Cat#345107, RRID:AB_10639737
APC conjugated c-kit (CD117)	eBioscience	Cat#17-1179-42, RRID:AB_10596820
Chicken anti GFP	Abcam	Cat#ab13970, RRID:AB_300798
Rabbit anti RFP	Rockland	Cat#600-401-379, RRID:AB_2209751
Mouse anti Stem121	TaKaRa	Cat#Y40410, RRID:AB_2801314
Mouse anti RET	R&D systems	Cat#MAB718-100, RRID:AB_2232594
Rabbit anti EDNRB	Biorbyt	Cat#orb37019, RRID:AB_10995764
Anti-rabbit IgG, HRP-linked	Cell Signaling Tech	Cat#7074S, RRID:AB_2099233
Rabbit anti LaminB1	Abcam	Cat#ab16048, RRID:AB_443298

REAGENT or RESOURCE	SOURCE	IDENTIFIER
Human anti ANNA-1	Gift from Dr V. Lennon	(King, Redden et al. 1999)
Donkey anti-Human IgG H&L (AMCA)	Jackson Immuno	Cat# 709-155-149 RRID: AB_2340529
Donkey anti-Human Dylight 405	Jackson Immuno	Cat# 709-475-149 RRID: AB_2340553
Donkey anti-goat IgG H&L (Alexa Fluor®488)	Invitrogen	Cat#A11055, RRID:AB_2534102
Donkey anti-mouse IgG H&L (Alexa Fluor®488)	Invitrogen	Cat# R37114, RRID:AB_2556542
Donkey anti-rabbit IgG H&L (Alexa Fluor®488)	Invitrogen	Cat#A21206, RRID:AB_2535792
Donkey anti-mouse IgG H&L (Alexa Fluor®555)	Thermo Fisher	Cat#A31570, RRID:AB_2536180
Donkey anti-rabbit IgG H&L (Alexa Fluor®568)	Invitrogen	Cat#A10042, RRID:AB_2534017
Donkey anti-goat IgG H&L (Alexa Fluor®568)	Invitrogen	Cat#A11057, RRID:AB_142581
Donkey anti-mouse IgG H&L (Alexa Fluor®647)	Thermo Fisher	Cat#A31571, RRID:AB_162542
Donkey anti-rabbit IgG H&L (Alexa Fluor®647)	Thermo Fisher	Cat#A31573, RRID:AB_2536183
Goat anti-chicken IgG H&L (Alexa Fluor®488)	Thermo Fisher	Cat#A11039, RRID:AB_142924
Goat anti-chicken IgG H&L (Alexa Fluor®555)	Thermo Fisher	Cat#A32932, RRID:AB_2762844
Chemicals, peptides, and recombinant proteins		
EDTA-free Protease Inhibitor	Sigma	Cat#11836170001
Y-27632	R&D Systems	Cat#1524
SB431542	R&D Systems	Cat#1614
BMP4	R&D Systems	Cat#314-BP
CHIR	R&D Systems	Cat#4423
RA	Sigma	Cat#R2625
FGF2	R&D Systems	Cat#233-FB/CF
Growth/Differentiation Factor-11, BMP-11	Peprotech	Cat#120-11
EDN3	American Peptide company	Cat#88-5-10B
AGN	Tocris	Cat#5758
GDNF	Peprotech	Cat#450-10
AA	Sigma	Cat#4034-100g
SHH	R&D Systems	Cat#464-SH
NGF	Peprotech	Cat#450-01
BDNF	R&D Systems	Cat#248-BDB
SCF	R&D Systems	Cat#255-SC-MTO
cAMP	Sigma	Cat#D0627
E8 medium	Thermo Fisher	Cat#A1517001
E6 medium	Thermo Fisher	Cat#A1516401
DMEM/F12	Thermo Fisher	Cat#21331020
Neurobasal medium	Gibco	Cat#21103049
N2	Stem Cell Technologies	Cat#07156
B27	Life Technologies	Cat#17504044
L-glutamine	Gibco	Cat#25030-164

REAGENT or RESOURCE	SOURCE	IDENTIFIER
MEM non-essential amino acids (NEAA)	Sigma	Cat#M7145
4',6-diamidino-2-phenylindole (DAPI)	Invitrogen	Cat#D1306
Critical commercial assays		
CytoSelect™ 24-Well Cell Invasion Assay, Basement	Cell Biolabs	Cat#CBA-110
iScript™ Reverse Transcription Supermix for RT-qPCR	Biorad	Cat#1708840
SsoFast™ EvaGreen® Supermix	Biorad	Cat#1725201
NuPAGE™ 4-12% Bis-Tris Protein Gels, 1.5 mm, 15-wells	Thermo Scientific	Cat#NP0336BOX
Trilogy	Cell Marque	Cat#920P-06
Deposited data		
RNA seq data	This study	GEO: GSE199439
ATAC seq data	This study	GEO: GSE199440
CUT and RUN data	This study	GEO: GSE199441
Experimental models: Cell lines		
Human embryonic stem cell (hESC) lines H9 (WA-09)	(Thomson, Itskovitz-Eldor et al. 1998)	RRID:CVCL_9773
Human embryonic stem cell (hESC) lines H1 (WA-01)	(Thomson, Itskovitz-Eldor et al. 1998)	RRID:CVCL_9771
Human embryonic stem cell (hESC) lines HUES6	(Cowan, Klimanskaya et al. 2004)	RRID:CVCL_B194
Human embryonic stem cell (hESC) lines MEL1	(Adewumi, Aflatoonian et al. 2007)	N/A
Induced pluripotent stem cell (iPSCs) lines 348.7, 706.3 and 864.3	(Cornacchia, Zhang et al. 2019)	N/A
H9 derived SOX10::GFP reporter line	(Chambers, Qi et al. 2012)	N/A
H9 derived SOX2::H2B-Tomato/ T::H2B-GFP dual reporter line	This study	N/A
H1 derived SOX2::H2B-Tomato/ T::H2B-GFP dual reporter line	This study	N/A
H9 derived mCherry reporter line	This study	N/A
H9 derived GFP reporter line	This study	N/A
Experimental models: Organisms/strains		
Mouse: NSG (NOD.Cg-Prkdcscid Il2rgtm1Wjl/SzJ)	JAX	005557
Mouse: B6.129S7-Ednrb tm1Ywa/FrykJ	JAX	021933
Mouse: NSG (NOD.Cg-Prkdcscid Il2rgtm1Wjl/SzJ)-Ednrb tm1Ywa/FrykJ	This Study	N/A
Oligonucleotides		
Hs_*SOX10*_1_SG QuantiTect primer assay	Qiagen	QT00055405
Hs_*FOXD3*_1_SG QuantiTect Primer Assay	Qiagen	QT00221928
Hs_*SOX2*_1_SG QuantiTect Primer Assay	Qiagen	QT00237601
Hs_*CDX2*_1_SG QuantiTect primer assay	Qiagen	QT00037807
Hs_*T*_1_SG QuantiTect Primer Assay	Qiagen	QT00062314
Hs_*GAPDH*_1_SG QuantiTect Primer Assay	Qiagen	QT00079247
Hs_*POU5F1*_1_SG QuantiTect Primer Assay	Qiagen	QT00210840
Hs_*NANOG*_1_SG QuantiTect Primer Assay	Qiagen	QT01025850

REAGENT or RESOURCE	SOURCE	IDENTIFIER
Hs_*WNT3A*_1_SG QuantiTect Primer Assay	Qiagen	QT00220542
Hs_*EDNRB*_1_SG QuantiTect Primer Assay	Qiagen	QT00014343
All other primers are listed in table S1	Qiagen and IDT	N/A
Software and algorithms		
FIJI	Open source Schindelin et al.,[117]	https://imagej.net/software/fiji
Flow Jo	FlowJo LLC	https://www.flowjo.com
DESeq2	Love et al[103]	https://bioconductor.org/packages/release/bioc/html/DESeq2.html
Prism 9	GraphPad Software	https://www.graphpad.com
Biorender	Biorender	https://biorender.com
Caseviewer	3dhistech	https://www.3dhistech.com/solutions/caseviewer/
Matlab R2014a	Open source	https://www.mathworks.com/company/newsroom/mathworks-announces-release-2014a-of-the-matlab-and-simulink-product-families.html